



# Building the Evryscope: Hardware Design and Performance

Jeffrey K. Ratzloff<sup>1</sup>, Nicholas M. Law<sup>1</sup>, Octavi Fors<sup>1,2</sup>, Henry T. Corbett<sup>1</sup>, Ward S. Howard<sup>1</sup>, Daniel del Ser<sup>1,2</sup>, and Joshua Haislip<sup>1</sup>

<sup>1</sup>Department of Physics and Astronomy, University of North Carolina at Chapel Hill, Chapel Hill, NC 27599-3255, USA; [jeff215@live.unc.edu](mailto:jeff215@live.unc.edu)

<sup>2</sup>Dept. de Física Quàntica i Astrofísica, Institut de Ciències del Cosmos (ICCUB), Universitat de Barcelona, IEEC-UB, Martí i Franquès 1, E08028 Barcelona, Spain

Received 2019 March 21; accepted 2019 April 9; published 2019 May 22

## Abstract

The Evryscope is a telescope array designed to open a new parameter space in optical astronomy, detecting short-timescale events across extremely large sky areas simultaneously. The system consists of a 780 MPix 22-camera array with an 8150 sq. deg. field of view, 13" per pixel sampling, and the ability to detect objects down to  $m_g' \simeq 16$  in each 2-minute dark-sky exposure. The Evryscope, covering 18,400 sq. deg. with hours of high-cadence exposure time each night, is designed to find the rare events that require all-sky monitoring, including transiting exoplanets around exotic stars like white dwarfs and hot subdwarfs, stellar activity of all types within our galaxy, nearby supernovae, and other transient events such as gamma-ray bursts and gravitational-wave electromagnetic counterparts. The system averages 5000 images per night with  $\sim 300,000$  sources per image, and to date has taken over 3.0M images, totaling 250 TB of raw data. The resulting light curve database has light curves for 9.3M targets, averaging 32,600 epochs per target through 2018. This paper summarizes the hardware and performance of the Evryscope, including the lessons learned during telescope design, electronics design, a procedure for the precision polar alignment of mounts for Evryscope-like systems, robotic control and operations, and safety and performance-optimization systems. We measure the on-sky performance of the Evryscope, discuss its data analysis pipelines, and present some example variable star and eclipsing binary discoveries from the telescope. We also discuss new discoveries of very rare objects including two hot subdwarf eclipsing binaries with late M-dwarf secondaries (HW Vir systems), two white dwarf/hot subdwarf short-period binaries, and four hot subdwarf reflection binaries. We conclude with the status of our transit surveys, M-dwarf flare survey, and transient detection.

*Key words:* telescopes – instrumentation: detectors – surveys – eclipses – (stars:) planetary systems

*Online material:* color figures

## 1. Introduction

Astronomical surveys searching for time-variable objects and events typically observe few-degree-wide fields repeatedly, use large apertures to achieve deep imaging, and tile their observations across the sky. The resulting survey, such as the Palomar Transient Factory (Law et al. 2009), Pan-STARRS (Kaiser et al. 2010; Tonry et al. 2012), SkyMapper (Keller et al. 2007), ATLAS (Tonry 2011), CRTS (Djorgovski et al. 2011), ZTF (Bellm 2018), and many others, is necessarily optimized for events such as supernovae that occur on day or longer timescales. These surveys are not sensitive to the very diverse class of shorter-timescale objects, including transiting exoplanets, young stellar variability, eclipsing binaries, microlensing planet events, gamma-ray bursts, young supernovae, and other exotic transients, which are currently only studied with individual telescopes continuously monitoring relatively small fields of view, or groups thereof. Short-timescale surveys including HAT (Bakos et al. 2004), SuperWASP (Pollacco et al. 2006), KELT (Pepper et al. 2007), and many others observe dedicated sky areas to reach very fast cadence and

good sensitivity, but at the expense of all-sky coverage. The Evryscope is designed to reach bright but rare events by optimizing for shorter-timescale observations with continuous all-sky coverage continued for many years.

The Evryscope (Figure 1) uses an array of 22 telescopes to cover the southern sky down to an airmass of  $\approx 2.0$  in each exposure. The system averages 5000 images per night with  $\sim 300,000$  sources per image. The Evryscope features mass-produced compact CCD cameras and lenses, and a novel camera mounting scheme to make a reliable, low-cost 0.8 gigapixel robotic telescope. We built the Evryscope at UNC Chapel Hill in early 2015 and deployed it to CTIO in Chile in 2015 May. The system has collected data continuously since first light in 2015 May. As of 2019 March, we have taken over 3.0M images resulting in 250 TB of raw data. The resulting light-curve database has light curves for 9.3M targets down to  $m_g = 15$  (and fainter for selected targets), averaging 32,600 epochs per target through 2018.

The Evryscope mounts an array of individual telescopes into a single hemispherical enclosure (the “mushroom”). The array



**Figure 1.** Evryscope, a two-dozen-camera array mounted into a 6-ft diameter hemisphere, deployed at the CTIO observatory.

(A color version of this figure is available in the online journal.)

of cameras defines an overlapping grid in the sky providing continuous coverage of 8,150 sq. deg. The camera array is mounted onto an equatorial mount which rotates the mushroom to track the sky with every camera simultaneously for 2 hours, before “ratcheting” back and starting tracking again on the next sky area (Figure 2). Each of the telescopes has 300 sq. deg. fields of view, 28.8 megapixels, and a 6.1 cm aperture. The Evryscope allows the detection and monitoring of objects and events as faint as  $m_g' = 16.5$  in few-minute exposures ( $m_g' = 15$ – $16$  under typical sky conditions) and as faint as  $m_g' = 19$  after coadding. The telescope specifications are given in Table 1.

The Evryscope has already contributed to a wide variety of science cases, ranging from precision studies of single targets (Tokovinin et al. 2018; Kosiarek et al. 2019; J. K. Ratzloff et al. 2019, in preparation), to statistical studies of stellar activity (W. Howard et al. 2019, in preparation), variable star discoveries (Ratzloff et al. 2019), hot subdwarf/white dwarf short-period binary discoveries (J. K. Ratzloff et al., in preparation), and transient discovery and follow-up (Howard et al. 2018; Corbett et al. 2018). In this paper, in addition to describing the Evryscope hardware, we also describe some of the first Evryscope discoveries from general stellar searches. Law et al. (2015) described the detailed Evryscope science cases. Subsequent papers will describe the data analysis pipelines in detail.

This paper is organized as follows. In Section 2 we explain the Evryscope system, design, and primary components. In Section 3 we describe the on-sky performance. Section 4 describes the transit detection methods, and shows example light curves and select first discoveries. We conclude in Section 5.

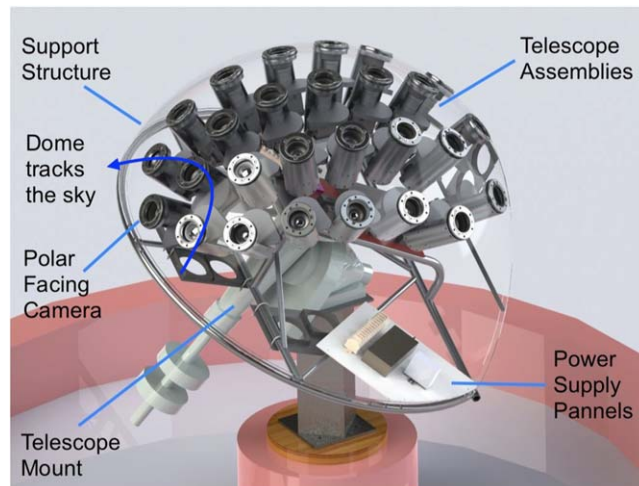


**Figure 2.** Cutaway rendering of the Evryscope showing the telescope mount, camera locations, and primary instrument components.

(A color version of this figure is available in the online journal.)

## 2. System Design

### 2.1. Science Requirements

The Evryscope’s science requirements were based on a study of the science possibilities for an all-sky telescope with an Evryscope-like design, detailed in Law et al. (2015) and summarized in Table 2. With 18 major science cases for the system, each of which having somewhat different needs, the setting of exact requirements was challenging. To constrain the design space and allow choices to be made, we settled on three simple requirements: a field of view (FoV) around 8,000 sq. deg., a  $3\sigma$  limiting magnitude of  $m_g' \simeq 16$ , a pixel scale sufficient to avoid crowding for 90% of sources above a galactic latitude of  $15^\circ$ , photometric precision better than 1% for bright stars, and the ability to co-add images to increase the target depth.

### 2.2. Overall Design

Starting with the general plan of an array of telescopes mounted together, we evaluated several concepts for the overall system design, including a flat tracking platform with each camera bolted to it, adjustable trusswork supporting each camera, and a spherical shape rotated around its polar axis (Law et al. 2012). We settled on a hemispherical dome mounted on an equatorial mount (the “mushroom”). This offered two advantages: (1) the camera support structure could be a single piece with no per-camera adjustment or alignment required and (2) the tracking mount, the single moving main structure, and therefore critical to reliability, could be a single off-the-shelf system. We summarize our overall design in Figure 2.

**Table 1**  
The Specifications of the Evryscope

Hardware	Description
Telescope mounts	27 (22 populated); shared equatorial mount
Telescope glass	61mm Rokinon F1.4 lenses
Mechanical mounting	Fiberglass dome with aluminum supports
Detectors	28.8MPix KAI29050 interline-transfer CCDs 7e- readout noise at 4 s readout time ≈50% QE @500nm; 20,000 e- full-well capacity
Field of view (Measured on sky)	8150 sq. deg. total (excluding ≈10% overlaps)
Sky coverage per night	18,400 sq. deg. (2–10 hours per night coverage)
Total detector size	780 MPix
Sampling	13"/pixel
Observing strategy	Track for 2 hours; reset and repeat
Data storage	All data recorded for long-term analysis ~50TB/year after all overheads
Performance	Description
PSF 50% enclosed-energy diameter	2 pixels in central 2/3 of FoV; 2–4 pixels in outer 1/3
Exposure time	120 s
Limiting magnitude	$m_{g'} = 16.0$ (3-sigma; 120 s exposure)
Photometric performance	1% photometry on $m_{g'} < 12$ stars every 2 minutes 6% photometry on $m_{g'} = 13.5$ every 2 minutes 10% photometry on $m_{g'} = 15.0$ every 2 minutes

**Table 2**  
The Evryscope Science Cases

Field	Description
Exoplanets	White dwarf transits and debris disks Hot subdwarf transits and debris disks Habitability-affecting superflares Eclipse timing exoplanet detections Confirmation of <i>TESS</i> single-giant-planet-transit events Long-period rocky exoplanets transiting M-dwarf stars
Stellar astrophysics	Low-mass-star rotation and activity Long-period eclipsing binaries for mass–radius relations Young-star activity and multiplicity Star-planet activity interactions Interacting binary outbursts Long-period dust dips
Transients	Gravitational-wave electromagnetic counterparts Microlensing exoplanet detection Galactic nova events Nearby, young supernovae Gamma-ray burst counterparts Fast-radio-burst counterparts

### 2.3. Camera Array Design

An Evryscope-type array telescope design has an enormous range of possible design choices. The choice of CCD array size must be traded off against the choice of lens, the point-spread function (PSF) quality available over the chosen array size, the pixel scale resulting from a particular lens/CCD combination,

and more subtle factors like vignetting and angular quantum efficiency. With the CCD detectors being the driving cost, the science requirement flowdown to the technical requirements was informed by a hardware-budget target of ≈\$300k.

#### 2.3.1. Lens and CCD Choice

With dozens of lenses and CCD arrays available from a multitude of manufacturers, we performed a comprehensive trade study of the possible lens/CCD combinations. The pixel scale was set by the anti-crowding science requirement to be smaller than 20", and we set the FoV to 8000 sq. deg. With those parameters fixed, we evaluated each lens/CCD combination based on the signal-to-noise ratio (S/N) that could be achieved all-sky on a  $m_{g'} = 16$  source. The S/N calculations included the likely PSFs and vignetting generated by each lens/CCD combination, the expected sky background and source photon noise contributions, the detector characteristics, and many other factors, and most lens/CCD combinations were not able to achieve the required S/N because of one of those factors.

We elected to limit our CCD selections to interline-transfer chips which have electronic shutters. Our prototype systems (Law et al. 2013) both suffered mechanical shutter failures during their arctic deployments, with the achieved number of error-free exposures being just over one-tenth of the specification. Although the failures were correctable by individually adjusting the tension of internal springs every few months, this is untenable in a robotic system with dozens of cameras. The

use of electronic shutters effectively eliminates this failure mode.

The trade study resulted in a single workable choice for lens/CCD combination: a Rokinon 85mm F/1.4 lens combined with a KAI29050 CCD array. All other combinations resulted in unacceptably low S/N or budgets factors-of-several times larger than our target amount. The KAI29050 array had a particular advantage in its rectangular format: most photographic lenses have rapid fall-offs in PSF quality towards the edges of the frame, and square arrays can therefore have poor image quality in the corners (Law et al. 2013). Compared with a square format, a rectangular array trades off highly off-axis image area at the corners for less off-axis area at the left and right edges of the array, and thus has more uniform PSFs across the image than a square CCD with equivalent area. On the basis of our positive experience with previous similar cameras, we elected to use thermoelectrically cooled Finger Lakes Instrumentation ML29050 units.

### 2.3.2. Camera Position Optimization and System Field of View

Next, we built a metric to optimize the camera positions in the array. Each camera produces a rectangular field on the sky, with a large enough FoV that spherical geometry must be taken into account for even simple sky-area calculations. We designed the camera array positions to (1) optimally tile over the above-airmass-two FoV and (2) avoid large areas of overlap between cameras; and (3) retain a few-degree overlap between each camera to constrain systematics.

We designed a code to project the FoV of each camera onto the sky, taking spherical geometry into account. The code then divides the sky into patches approximately  $0.3^\circ$  across, counts the number of cameras pointed at each patch, and measures the total sky area and overlap areas covered between different combinations of cameras. Starting with a simple arrangement of cameras divided into rows of declination, we then varied the position of each camera in the array using an annealed downhill-simplex algorithm, optimizing for overlap and covered sky area (Law et al. 2016). The optimization converged on an arrangement very similar to the input declination-separated grid of cameras; other camera arrangements we explored did not produce significantly better performance metrics. For ease of fabrication we used the simple declination-separated grid to place the cameras, with spacing parameters inherited from the fully optimized solution (Figure 3).

Each camera assembly rotates in a circular arc around the pole-facing camera as the mushroom tracks the sky. Over the course of a typical night the system covers  $\approx 18,000$  sq. deg. (Figure 4), with each part of the sky being observed at 2-minute cadence for 4–10 hours per night.

Each CCD is orientated so that its long axis (designated as the x-axis) is tangential to this arc; this ensures the objects in

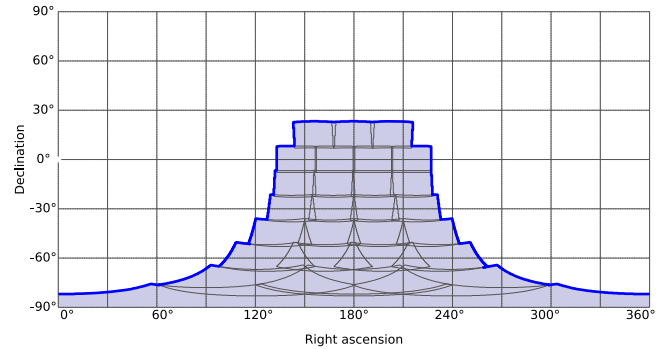


**Figure 3.** Evryscope camera placement when deployed at the CTIO observatory (some of the northern camera spots are currently unpopulated). (A color version of this figure is available in the online journal.)

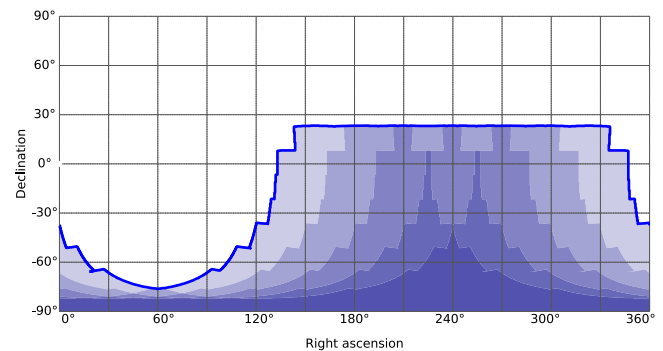


**Figure 4.** 18,000 sq. deg. coverage of the system over a single night. The depth of coloration corresponds to the number of two-hour ratchets covering each part of the sky; each ratchet includes 60 2-minute epochs. (A color version of this figure is available in the online journal.)

each image remain in a constant orientation throughout the night. There are seven rows, with the cameras in each row sharing the same pointing declination, equidistant from the pole camera. The camera mounting flanges (and therefore the CCDs) are normal to the surface of the mushroom dome, which ensures that the cameras are pointed in the proper direction without manual alignment being necessary. We designed the mushroom to be capable of supporting 27 telescopes; at CTIO 24 are Southern hemisphere facing and three cover positive declinations. The number of operational cameras has varied slightly during the course of the project: 22 or 23 cameras have been operational in 2015–2017, with another camera reserved for testing. We plan to fill in all available slots in the near future.

### 2.4. Telescope Structure, Tracking, and Image Quality Optimization

Mechanically, the Evryscope consists of an array of cameras mounted into a hemisphere (the mushroom), which in turn is

mounted onto a German equatorial mount which keeps all the cameras tracking.

#### 2.4.1. Camera Hardware Units

The camera hardware units fix the cameras to the mushroom, provide mechanical support of the components, and a mount for a protective window. The camera mounts have three primary constraints on their design: flexure limits, size, and weight. Although atmospheric refraction precludes keeping each star on the same pixel while tracking (Law et al. 2015), we designed the camera mounts to not contribute any extra drift throughout the Evryscope’s range of motion, requiring the relative camera mount flexure to be less than  $13''$ . The size of the mushroom was set to a 6-ft diameter by our target dome, and this set the packing requirements for the cameras. As there are two dozen camera mounts with relatively heavy CCD units, they and the systems they contain are the primary drivers of the weight of the system. A trade study of available mounts suggested that significant cost savings were possible if the total mushroom weight could be kept below 400 lbs.

We used 3D modeling to test several hardware unit designs, with the goal to minimize weight, flexure, and complexity. The final version (Figure 5) features interlocking sections for added rigidity, weighs less than 4 lbs (supporting imaging hardware that weighs 8.0 lbs), and provides a maximum differential flexure of less than 10 arcsec. The maximum flexure in the vertical orientation is  $\approx .02$  mm and over the course of a telescope ratchet the differential movement due to the changing camera orientation is well within our 1 pixel goal. The camera mounts are interchangeable, have locator pins to easily place the cameras into the proper orientation in the mushroom, and perform equally well in flexure for all cameras regardless of the declination row (which have considerably different gravitational vectors).

Each mount has an outer window to protect the lenses and electronics from dust, water, and other possible contaminants, enabling easy cleaning as well as providing a backup to the observatory dome. The high transmission (over 96% in the visible range) optical window is mounted on a soft o-ring with a stainless steel retaining ring, and allows for easy cleaning of dust during maintenance.

Interline-transfer CCDs cannot take darks without extra mechanical shutters, so we elected to use a filter wheel with a blocked position to allow calibrations to be taken. The Finger Lakes Instrumentation CFW-5-1 filter wheels also provide a sunshield (Section 2.7.4) and science filter changing capability.

#### 2.4.2. Precision Lens/CCD Alignment Systems (“Robotilters”)

Camera lenses are used on SuperWASP (Pollacco et al. 2006), HAT (Bakos et al. 2004), KELT (Pepper et al. 2007), XO (McCullough et al. 2005), and other transiting exoplanet surveys to reach as much as 1000 sq. deg. fields of view. Other

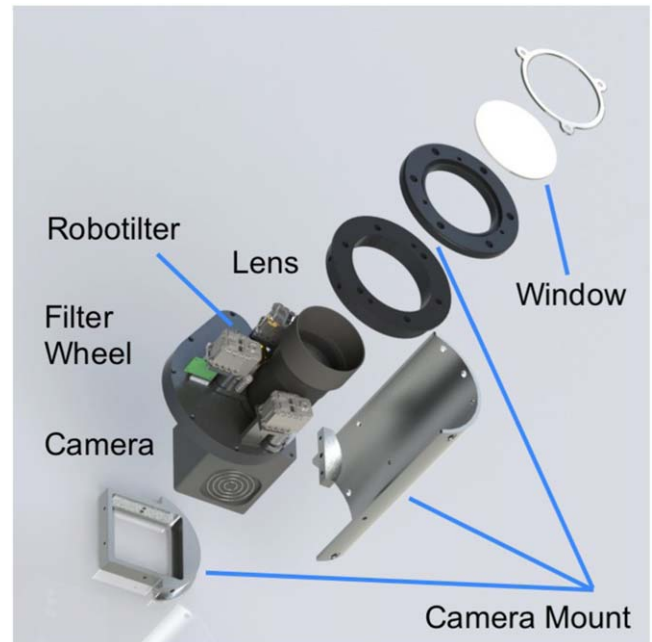


**Figure 5.** Evryscope unit camera assembly

(A color version of this figure is available in the online journal.)

surveys types such as the ASAS-SN (supernova) (Shappee et al. 2014), Pi of the Sky (gamma-ray bursts) (Piotrowski et al. 2013), Fly’s Eye (asteroid detection) (Csépany et al. 2013), and HATPI<sup>3</sup> also use camera lenses to reach wide sky coverage. These types of wide-field surveys and many others including the Evryscope are susceptible to image quality tilt and focus challenges. Even a slight misalignment between the optics and the CCD causes a tilt that results in an unacceptable increase in size of the PSF FWHM toward the edges and corners of the image. For the Evryscope, the very wide FoV (380 sq. deg.), fast F# of each lens and the small  $5.5 \mu\text{m}$  pixels exaggerate this effect. While the machining tolerances ( $\pm .005$  inch in most cases) and the assembly tolerances of the mass-produced lenses, adapters, filter wheels, and CCD assemblies is reasonable for their standard usages, it is not precise enough to achieve the absence of tilt required for the needed Evryscope image quality.

We designed a robotic tilt adjustment mechanism (Figure 6) to address those challenges, with the ability to remotely and precisely realign the camera assemblies. The Robotilter (Figure 6) uses three precision servos controllable to within 4 deg. steps coupled to an 80 thread per inch adjuster to move the lens position relative to the CCD. This allows adjustment of the tilt as well as the lens/CCD separation in increments as fine as .003 inch. The design uses specialized flexible shaft couplings to prevent binding and tension springs to hold the

<sup>3</sup> <https://hatpi.org>

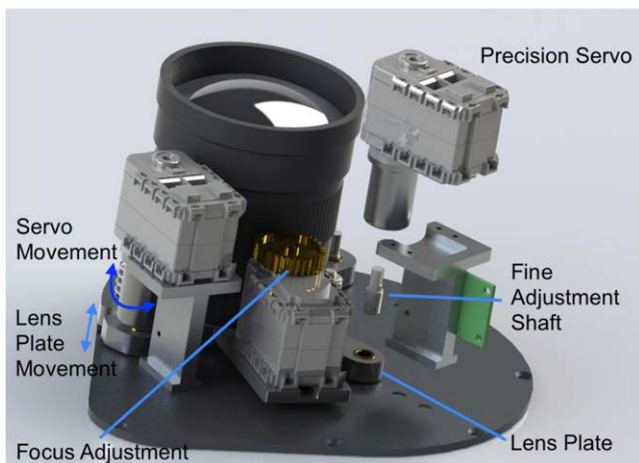


**Figure 6.** Robotilter automated tilt/alignment/focus system  
(A color version of this figure is available in the online journal.)

lens accurately in place. The assembly mounts to the top plate of the filter wheel to avoid costly re-configuring of the existing filter wheel, CCD, or camera mount. A separate servo independently adjusts the lens focus position to compensate for tolerance differences due to temperature changes throughout the year. The Robotilters were installed in 2015 November and the cameras were aligned remotely in early 2016; the installation of the Robotilters was the final step in commissioning the system. The Robotilters and resulting image improvements will be described in detail in an upcoming technical paper (J. K. Ratzloff et al. 2019, in preparation).

#### 2.4.3. Mushroom Structure and Wind Shake

The camera support structure (the mushroom, Figure 1) needs to provide the same limited flexure as the camera mounts, while also bearing the 400 lbs load of up to 27 camera assemblies and related components. We chose a molded fiberglass hemisphere with support ribs along the bottom and back for extra strength and rigidity, and a sturdy mounting point. The material is hand-laid cloth weave fiberglass, providing light weight and minimal flexure with excellent durability. The mushroom also features reinforced and precision-located inner and outer camera mount flanges to provide accurate and secure mounting points. The camera flanges are normal to the surface, and the holes are CNC cut into the mushroom to ensure the precise location necessary to achieve the desired field coverage without holes or excessive overlap. The manufacturing tolerances are .020 inch on the hole locations, and based upon this the camera alignment is fixed normal to the mushroom surface and the long side CCD is perpendicular to the rotation axis. Our 3D model simulation predicts that despite the close packing of the cameras and considerable weight, the stress is mostly compression and



**Figure 7.** Mathis German Equatorial mount, the tubular base structure, and the mounted mushroom—showing the instrument inset, mass alignment, and camera accessibility.

(A color version of this figure is available in the online journal.)

results in absolute movements on the scale of .02 mm. Differential camera movements over the tracking cycle are on the order of microns ensuring accurate camera pointing. On-sky pointing accuracy is well within the simulated performance.

The hemispherical shape of the mushroom, along with the placement of the instrument so that the dome leaves in the open position are slightly higher than the mushroom base, help make the Evryscope resilient to wind shake. The system is able to operate in 30 mph winds without a measurable change in image quality.

#### 2.4.4. Tracking Mount

The base structure (Figure 7) attaches the mushroom to the Mathis 750 mount, via a mount plate attached to the tracking mount and a structure which transfers the mechanical load from the mushroom fiberglass. We tested several design ideas via finite element analysis and found a reinforced round tubing design to be most effective. Using aluminum tubing, we reduced the weight in half from a similar design made of steel and kept the total flexure within requirements. The differential camera displacement of the mounting base throughout the telescope tracking is on the order of microns, and combined with the mushroom and camera mount flexure is simulated to be within our total goal of 1 pixel, with comparable performance measured on-sky.

The proper location of the center of mass is critical to reliable telescope mount operation. We inset the mount plate significantly into the mushroom so that the effective lever arm of the Evryscope cameras is minimized (Figure 7). The center of mass is only 10 inches from the mount plate, which greatly reduces the load on the telescope mount compared to simpler designs. The base structure positions the Evryscope so that the center of mass in the mounted position is directly over the

telescope mount axis center, further reducing stress on the telescope mount and easing the balancing of the instrument.

The polar alignment of the mount is critical to the tracking performance of the system. Because the system's FoV is such a large fraction of the sky, conventional pointing models cannot be used, because they optimize the performance on one part of the sky by reducing performance on other parts of the sky. For this reason, we developed a precision polar alignment procedure specifically for Evryscope-like instruments ([Appendix](#)).

On-sky performance confirms the predictions of the flexure and center of mass simulations. The camera pointing is accurate within a tenth of a degree, providing the proper FoV overlaps without gaps (except for one initial, now corrected, misalignment caused by a contaminated bolt thread). The camera orientations remain constant throughout sky tracking. The telescope mount tracks the sky consistently without stalling or shifting, and we conclude that the total flexure is very close to the 1 pixel goal.

#### 2.4.5. Dome

The Evryscope is located in an AstroHaven clamshell dome originally built for the PROMPT network of telescopes (Reichart et al. 2005). The dome had already been used for routine long-term operation, and no mechanical changes beyond a custom pier structure were necessary for the Evryscope deployment. Careful electrical design was necessary, however; the large dome opening/closing motors can induce strong transients onto power and potentially signal lines from the dome. To avoid possible interference or even damage, we separated the dome electrical systems on a separate UPS system. A Raspberry-Pi single-board computer runs the dome-control daemon and communicates with the rest of the system via an electrically isolated Ethernet connection; there are no other direct electrical links between the Evryscope and the dome.

#### 2.4.6. Observatory Site & Weather-related Design

The Evryscope is deployed at CTIO in Chile in PROMPT (Reichart et al. 2005) dome 4 (Figure 8). The site was chosen for the large number of usable nights (>320 per year), dark-sky conditions ( $m_v = 21.8$  moonless night background average), and Southern sky visibility. UNC affiliated hardware and support synergies, especially the PROMPT Program, were also advantageous.

The dome and observatory site introduced several design constraints: (1) a maximum power consumption of 15A/120V; (2) operation with a relatively small Internet bandwidth that precludes the real-time, off-site transport of data; (3) the potential for lightning strikes and earthquakes (Section 2.7); (4) potential external temperature ranges of  $-15^{\circ}\text{C}$  to  $+25^{\circ}\text{C}$ ; and (5) extremely dry conditions.



**Figure 8.** Evryscope in PROMPT dome 4.

(A color version of this figure is available in the online journal.)

The low end of the temperature range is outside that which most off-the-shelf electronics are rated for. Wherever possible, we purchased industrial components rated for low-temperature operation (typically  $-20^{\circ}\text{C}$ ). In some cases, we tested and used off-the-shelf consumer electronics (for example, Raspberry-Pi single-board computers); testing was performed in fridge-freezer units under a range of relative humidity (see Law et al. 2013; Law et al. 2016 for testing details).

The potential for extremely dry weather spells required careful electronic and mechanical design. For example, Nylon becomes brittle under extremely dry conditions (Pai et al. 1989); this can cause failures in cable insulation and zip-tie-type harnesses in a matter of months, leading to possible short circuits or mechanical interference between cables and moving parts. The static electricity discharges prevalent in dry conditions can cause electronic failures, especially while personnel are maintaining the system. Many power supplies and similar units are rated only to 20% relative humidity, while the CTIO site can regularly reach low-single-digit humidity. We mitigated these concerns by using only plastics, connectors, and electronics rated for long-term extremely dry conditions. All metal components are grounded, with isolators used to avoid ground loop conditions, and we take operational steps to ground personnel before working on the system.

## 2.5. Electrical and Electronic Design

The Evryscope mushroom contains over 600 ft of cabling, with further ancillary systems located outside the main telescope body. Figure 9 shows an overview of the power and data paths within the dome.

### 2.5.1. Power Distribution

The Evryscope cameras together require a maximum of  $\approx 170\text{A}$  of 12V power; the ancillary systems with the mushroom (Robotilters, filter wheels, fans, USB hubs, etc.) together

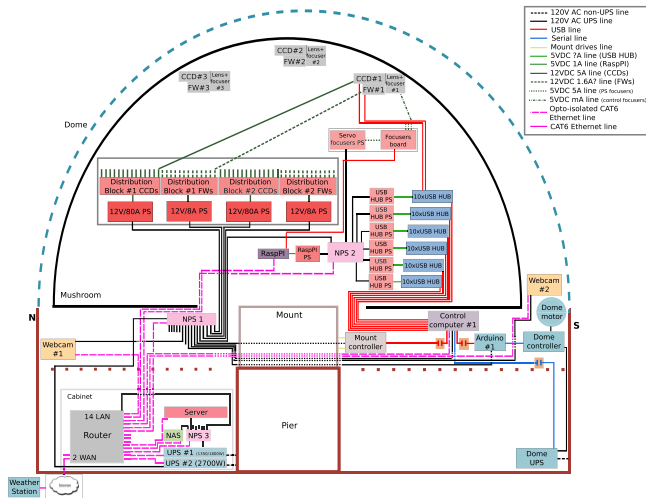


**Figure 9.** Evryscope Wiring Diagram.  
(A color version of this figure is available in the online journal.)

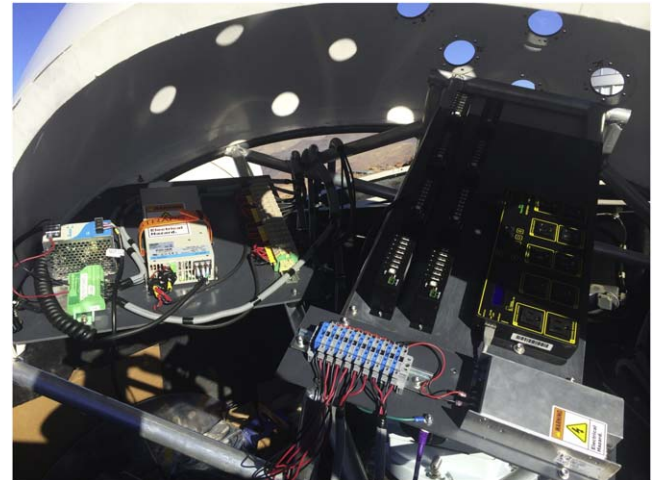


**Figure 10.** Power supply panels; left is the camera and filter-wheel power/distribution and the right is the USB hubs and NPS.  
(A color version of this figure is available in the online journal.)

require a further  $\approx 20A$  of 12V power. The AWG-1 (quarter-inch diameter) cables required to safely carry the required 200A into the mushroom would be bulky and inflexible, and risky if frayed or overheated. Powering each camera from its own 12V supply would lead to a very bulky and heavy power distribution system, beyond the load capacity of the mushroom mount. For those reasons we elected to send 120V AC power into the mushroom over a single flexible small-diameter cable, and use two 120A-capable 12V power supplies to power the main camera systems. We deliberately overspecified the power supplies to reduce the need for active cooling and the associated vibrations. Ancillary systems are powered from their own smaller 12V power supplies, with Digital Loggers Network Power Switches allowing computer-controlled switching of each component. Although it has proven reliable, this setup resulted in over 600 ft of cabling inside the main mushroom, because each camera has six separate cables going into it (3 power, 3 data). These cables are heavy and impede airflow; the Northern Evryscope, currently under commissioning, has relay and control systems built into each camera to reduce the number of required cables to two per camera.

The two 120V input/12V 80A output power supplies are mounted on panels attached to the wings of the base inside the mushroom (Figure 10). Fused distribution blocks with custom cabling connects the power to the cameras. The filter wheels use a similar, but smaller, 120V input/12V 8A output power and distribution located on the same panels. An additional 120V input/12V 8A output power supply is also available on each panel to supply the focus servos, cooling fans, and other accessories. A panel attached to the center of the base over the mount (Figure 10) holds a Network Power Supply (NPS) and a power supply for the USB hubs used to control the cameras

assemblies. The selection and placement of the power systems allows for proper balancing of the mushroom assembly, cooling of the electronics, access to all of the components, and provides a safe supply of power to many different systems confined in a small area.

### 2.5.2. Cooling

The Evryscope uses up to 1.2kW when all cameras are cooling at maximum power, producing a significant amount of heat within a 6-ft semi-enclosed space. In-lab tests showed that parasitic heating between cameras could lead to a thermal runaway under some environmental conditions: cameras pulling in warm air exhausted by the thermoelectric coolers of neighboring cameras must work harder to cool their sensors, increasing the amount of waste heat exhausted, and causing other cameras to further increase their cooling power. This process headed for runaway when the air temperature inside the mushroom exceeded  $\approx 32^\circ C$ . Although several layers of protection prevent hardware damage from overheating (Section 2.6) this could have impacted system uptime during summers.

We implemented three systems to eliminate the parasitic heating. First, we built aluminum deflectors to move the camera exhaust air toward the center of the mushroom. Second, we added a bank of 8 120 mm low-vibration 12V fans to direct cool air to the top of the mushroom. Third, we added external Vornado high-volume industrial fans to direct large amounts of external cool air to the mushroom (when rarely necessary). Together, these systems produce a coherent flow of cool air from the front-bottom of the mushroom to the top of the dome and down again out of the back of the systems. Testing showed no measurable effect on image quality when all systems are



activated. The thermal protection systems have not triggered a shutdown since this system was commissioned.

### 2.5.3. Environmental Monitoring

We monitor the hardware status with sensors distributed around the mushroom and dome, all linked to the main control system via Ethernet or USB connections. The main control computer runs automated analysis and control scripts, and alters the state of fans as necessary to maintain stable temperatures around the cameras. Logs of all sensor values are recorded each minute.

Inside the mushroom, each camera has an external temperature sensor, measuring the air temperatures at 22 points around the dome. An environment-monitoring Raspberry-Pi is located at the center of the mushroom. Its custom-built sensor board monitors the overall mushroom temperature with a wide-angle infrared thermometer, the center-mushroom temperature with a built-in sensor, and the tilt of the mushroom using a precision three-axis accelerometer. A timing GPS system is also connected at that location. A summary of all sensors is shown in Table 3.

Outside the mushroom, two webcams continuously monitor the system from the north and the south. The northern webcam is a pan/tilt unit; the southern webcam is a Raspberry-Pi camera which, in addition to providing a view of the mushroom internals, automatically monitors the light level in the dome. If the light level is consistent with the dome being unexpectedly open in daytime, a loud alarm bell is sounded and the Evryscope team is alerted via email.

We use the PROMPT weather monitoring system (Reichart et al. 2005) for dome open/close decisions; this system has been in reliable operation for almost a decade. The PROMPT weather station monitors cloud levels, wind, and dewpoint. We use the RASICAM (Lewis & Howard Rogers 2010) system to log cloud measurements for data-quality testing.

### 2.5.4. Data and Control Signal Distribution

The main control computer, watchdog, and environment-monitoring computers and data storage and analysis servers are located within the telescope dome, with optical fiber connections to a backup storage site in an adjacent PROMPT dome. The Evryscope data and control bus is a gigabit Ethernet system operating as a separate subnet behind a router connected to the main CTIO network.

A single sealed and fanless Logic Supply ML600G-30 rugged computer runs the robotic control software (Section 2.6) and the USB-controlled devices, including the cameras, filter wheels, Robotilters, and the mount.

Over 50 individual USB devices are connected to the control computer, which produces challenges to reliable system operations (Ethernet control was not available for our chosen cameras at the time of system design). We initially connected

**Table 3**  
The Evryscope Environmental Monitoring Sensors

Description	Location
Mushroom interior temperature	22 sensors in cameras
Overall mushroom temperature	Watchdog RasPi
Mushroom electronics temperature	Watchdog RasPi
Three-axis-accelerometer tilt	Watchdog RasPi
GPS timing sensor	Watchdog RasPi
Webcam dome light level sensor	Dome control RasPi
Rain sensor	Dome control RasPi
Smoke detector	Dome floor
Pier-base temperature sensor	Mount controller
Weather station	PROMPT array

groups of 4–8 USB devices together using powered USB hubs. However, lab testing showed occasional USB-bus-voltage brownouts, where the 5V power supply in a typical computer could be pulled out of voltage specification just by connecting dozens of USB devices, even when the devices were powered off and connected via powered hubs. This could prevent the control computer starting up or cause unreliable operation, and occurred for all tested brands of USB hubs. We eliminated this problem by finding and removing an undocumented jumper inside Starlink ST7200USBM rugged USB hubs which completely disconnects the upstream USB power rails from the downstream devices; this produces reliable operation with at least 60 USB devices connected.

### 2.6. Robotic Control Software

The Evryscope is controlled by custom Python framework running on several computers within and outside the mushroom. We use a daemon-based software model, where each subsystem is controlled by an individual script operating as a separate process; this ensures that crashes related to individual hardware components do not stop the control of the other components. Critical systems such as emergency watchdogs are located on separate computers, allowing the entire system to enter a safe mode in an emergency even if the main control computer is disabled. The 18 daemons comprise 18,000 lines of Python code and communicate via a JSON-based protocol on TCP/IP sockets.

A supervisory daemon is responsible for overall control, working as a finite-state machine to decide on the current best system operation mode from a range of options (science operations, taking calibrations, waiting for good weather, waiting for sunset, resetting mount for the next ratchet, and emergency shutdown mode). Transitions between modes are handled automatically by issuing commands to the relevant daemons and waiting for confirmation of hardware states as necessary. Commands to the hardware daemons range from simple (changing a filter position for example), to complex operations that can take many hours and involve large amounts

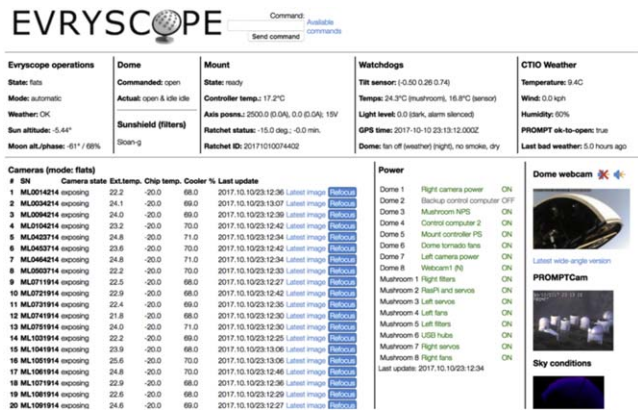


**Figure 11.** Evryscope status webpage, used for system monitoring and control. Commands can be issued to each hardware and software system using buttons or a simple text interface. (A color version of this figure is available in the online journal.)

of computing resources (executing a 3D-surface focus map for a camera, for example). A manual mode allows humans to issue commands directly to each daemon as necessary using the Evryscope status webpage (Figure 11), although the supervisory daemon must be informed, or the unexpected hardware states will be detected as error conditions.

The system is designed to fail safe, entering a safe mode on all important errors. Each subsystem daemon is responsible for the safety of its individual hardware components. This is relatively trivial in the case of filter wheels and similar low-impact systems, but is safety-critical for some components like the dome, the camera power supplies and the tracking mount. To produce a fail-safe mode, where the hardware is protected in the case of a system error or unexpected condition, the supervisory daemon issues a “heartbeat” ping to each daemon every 15 seconds. If the ping is not received on schedule, each individual daemon enters a safe mode—closing the dome, powering off the cameras, placing the filter wheels into sunshield position (Section 2.7.4), and so on. Conversely, if a daemon does not respond to the heartbeat ping, suggesting it has crashed, the supervisory daemon triggers an error condition and stops issuing heartbeats to the other daemons. On any unhandled error condition the entire system enters semi-safe mode within  $\approx 15$  s (dome closed, mount stopped), and fully safe (sunblocks enabled, cameras powered off) within a minute. When this occurs, an email is sent to the Evryscope team for manual checks. This typically occurs once every few months, usually because of a communications glitch with an external component.

## 2.7. System Robustness and Failure Mode Mitigation

The Evryscope is designed for fully robotic operation with minimal on-site support. A rigorous analysis and mitigation of

potential failure modes is vital to ensure robust operation. We categorized possible failure modes into a) problems that would allow the system to keep running with degraded performance and b) catastrophic failures that could cause permanent hardware damage. For the first type, we designed the system control software to monitor all hardware systems continuously and fail safe into a known-good state on detection of errors (see Section 2.6). For the potentially catastrophic problems, we designed multiple redundant backup systems.

### 2.7.1. Fire

The Evryscope uses up to 1.2kW of power when all systems are simultaneously operating, within a fairly small enclosure. Two 120A/12V power supplies supply power to the camera systems, and a short-circuit on a 120A-capable line could easily produce enough heat to ignite surrounding material. We mitigated these concerns by (a) breaking apart the high-current lines very close to the power supplies for individual camera power; (b) individually fusing each power supply line; (c) powering the system via GFCI breakers to produce a rapid shutdown in the event of a ground fault; (d) specifying all plastics to be flame retardant; (e) wrapping all exposed cables in flame-retardant material; (f) placing an omni-directional infrared temperature sensor in the dome which shuts the power down on detection of an overheat condition; and (g) placing a Raspberry-Pi connected smoke detector in the dome to rapidly shut off power and sound an alarm if smoke is detected.

### 2.7.2. Lightning

Electrical storms are rare at CTIO, but the Evryscope has so far experienced one extremely nearby lightning strike that damaged equipment in nearby domes. To mitigate the possible lightning impact, we applied surge protectors to every power line and isolators to every USB and Ethernet cable longer than three feet; this also mitigates the effects of possible ground loops. No lightning damage has been experienced by the system.

### 2.7.3. Earthquakes

Chile regularly experiences large earthquakes, and telescope systems must be designed to survive large ground accelerations. As with the other main instrument components (Section 2.4), we evaluated the Evryscope pier mount design using 3D modeling finite element analysis. We simulated the telescope weight on the pier design over several angles to mimic positions during the ratchet cycle. The final pier design is 1/2" wall structural grade steel box tubing, with a strength failure several orders of magnitude above any level the Evryscope is likely to see. An accelerometer inside the mushroom measures the tilt of the mushroom and any other accelerations, and places the system in safe mode if limits are

exceeded. On 2015 September 16, CTIO was hit by a 8.3 magnitude earthquake at a distance of 115 miles. The Evryscope automatically went into safe mode; no structural damage occurred and after quick manual checks, the system was able to restart with no maintenance required.

#### 2.7.4. Sun Exposure

With a telescope pointing at almost the entire sky, if the dome is opened during the day at least one camera would be pointing directly at the Sun. The resulting heat buildup in the Sun-pointing region of the CCD chip would be likely sufficient to cause significant CCD damage. If the dome was left open for an entire day, during maintenance or as a result of equipment failure, it is possible that an entire row of cameras could be damaged or destroyed. We addressed this with 1) a daylight alarm which sounds a loud bell and contacts the Evryscope team; 2) sunshields built into each camera.

The sunshields are contained within the cameras' filter wheels and consist of a 3mm-thick steel washer backed by a mirror; sunlight entering the lens will be very out of focus at the filter position, preventing the formation of hotspots. Experiment at Chapel Hill showed no dangerous heating of the lens over hours of Sun exposure. The sunshields are a primary safety system and as such are engaged immediately upon error conditions; each morning the system engages the sunshields as part of the shutdown procedure (apart from fans, the sunshields are the only moving parts inside the mushroom that are used nightly).

## 2.8. Data Analysis

Here we describe briefly the Evryscope data analysis pipeline, forced-aperture photometry, and light-curve generation; a full description will be published in upcoming work (H. Corbett et al. 2019, in preparation). As with many wide-field surveys, the Evryscope data analysis platform adapts established methods into a custom solution. The extremely wide field, concomitant optical distortions and flat-fielding challenges, and the very large quantity of data are the primary challenges. Each night, the Evryscope opens up and takes calibrations and science images automatically. 15–20 darks and twilight flats are taken each night for each camera and on a typical observing night, with good weather, each of the 22 cameras will take 250–300 science images.

### 2.8.1. On-site Data Analysis Infrastructure

The Evryscope generates approximately 6500 55 MB science images each night. This data volume precludes transmitting the data for off-site processing with the current CTIO Internet link. All data is therefore stored and processed on-site. Images are stored in an FPACK-compressed format across multiple Synology DS-2415+ network storage

appliances, each of which is equipped with twelve 8 or 12 TB drives. In addition to image storage, we have provisioned a separate data store exclusively for our photometry database, consisting of 12 helium-filled 8 TB drives directly attached via a SAS backplane to our database server.

Data processing is split between two servers, both housed in the PROMPT domes at CTIO. The original server, a 12-core Intel Xeon-based machine, was installed with the system. Post deployment, the mainboard of this server suffered some mechanical damage, limiting its RAM capacity to 112 GiB. In January of 2016, a second server was installed and the original was reprovisioned to support a calibrations and image indexing database, while all other analysis tasks were migrated. The second server is also based on the Intel Xeon platform, with 36 physical cores and 256 GiB of RAM.

### 2.8.2. Pipeline Design

The Evryscope currently runs a forced-aperture-photometry pipeline. The pipeline takes incoming images, calibrates them with darks and flats, generates a precision astrometric solution from the bright stars; estimates local background light and noise across each image; and measures aperture photometry for all sources from a reference catalog. The Evryscope pipeline consists of ~50,000 lines of custom Python and C++ code, with custom code performing flat-fielding; astrometric distortion correction; local background and noise estimation; precision aperture photometry; transient detection; and large-volume data storage. We expect to upgrade the pipeline to full image subtraction in the future.

We extensively tested standard data analysis software with Evryscope images (for example, the SExtractor (Bertin & Arnouts 1996) and astrometry.net (Lang et al. 2010) software suite used in PTF (Law et al. 2009) and the AWCams (Law et al. 2013)). However, we found that the standard software struggles with our crowded images with large lens distortions: astrometry.net had a >20% probability of failing to find a good astrometric solution at the edges of the frames, often producing distortion solutions several pixels off. SExtractor often could not attain a good background noise estimate for our crowded images, and therefore set the source-detection requirements extremely high; often several-degree-wide regions of the Evryscope images did not show any detections despite tens of thousands of stars being clearly visible by eye. A few percent of the Evryscope images also showed SExtractor photometry very divergent from adjacent images, with stars' brightness measurements changing by tens of percent with no discernible by-eye difference in the input images; these problems persisted regardless of the input settings. For these reasons we developed a completely custom pipeline, although we do use astrometry.net for initial rough astrometric solution and SExtractor for quick source-detection for camera focusing; both codes work very well for those applications.

Each processed night consists of  $\approx 360$ GB of raw imaging data, resulting in several hundred new data points for each of  $\approx 10$ M stars. On our current computing hardware, the pipeline is capable of processing  $\sim 7$  nights (2.5 TB of imaging data) every 24 hours. This speed is necessary to allow us to re-reduce our current three-year data set in a reasonable time.

### 2.8.3. Image Quality Checks and Calibrations

Each Evryscope science image is subjected to an initial quality control script which evaluates the image quality based on the presence of stars in the image, PSF shape (avoiding rare tracking errors), and background levels. Images that pass ( $>90\%$ ) are masked for known bad pixels and columns.

Darks are taken daily with the filter wheel in the closed position, and monthly midnight darks are taken for comparison to check for light leaks. Masterdarks are generated by combining and median averaging several hundred darks. Our CCD characteristics are sufficiently stable to use the masterdarks for a season.

Twilight and sunrise flats are taken daily and evaluated with a quality control check for stars and clouds. Residual point sources are removed. Lens vignetting and small-scale interpixel variation in CCD sensitivity are removable to the 1% level with standard flattening procedures, however the large-scale sky gradient due to the extremely wide FoV necessitates a more complex procedure. We constrain the large-scale variations on using on-sky photometric measurements of starfields, and measure the small-scale variations from the high-frequency structure in twilight flats.

### 2.8.4. Photometry and Light Curves

Our current data set includes 9.3M stars with an average of 32,600 photometric measurement points. The photometric points are stored in a flat-file-based custom backend storage system written in Python. The system is partitioned by sky position using HEALPix pixels (Gorski et al. 2005). HEALPix pixels divide the sky into equal area regions; we selected a 3.5 sq. deg. HEALPix pixel size for convenience to limit the number of stars in a particular region. This aids in processing of the light curves (done per HEALPix pixel) and allows for multi-threading and tiling the database writing steps. We evaluated database management systems (DBMS), but found that for our extremely consistent-format numerical data our custom system could reduce storage requirements by a factor of five compared to PostgreSQL while increasing access speed by a factor of 10. We also evaluated similar commercial and open-source flat-file numerical data storage systems and found that the performance was generally comparable to our flat-file-based system, but with significantly higher implementation complexity and programming overhead. The flat-field storage system stores approximately 15 TB/yr of light-curve data.

Each star's photometry is measured in five different photometric apertures, allowing an optimization of the S/N for each star (for example, selecting larger apertures for brighter stars; this technique is used by several surveys, e.g., Pollacco et al. 2006). Each measured data point also includes the star's measured R.A. and decl., CCD position, estimated S/N, limiting magnitude at that point, background light level, peak flux level, and a GPS-based precision timing signal with tested 1 s accuracy (Corcoran et al. 2018).

We periodically generate precision light curves for each star based on the typically tens of thousands of photometric points recorded for each star. The light-curve generation code processes each HEALPix pixel separately, performing differential photometry on the contained group of several thousand stars. Atmospheric extinction variations from clouds and airmass are corrected for using differential photometry among the thousands of stars in each HEALPix pixel. First, images pass through an image quality check which rejects images with high background, low numbers of detectable sources, or suspect PSF shapes. Next, the least-variable stars are automatically selected to form a consistent set of reference stars (this procedure is iterated with the differential photometry to find the stars most indicative of the overall photometric variations). For each single-camera image accepted by the pipeline for processing, which typically have a few 100,000 stars, each source is checked for possible blending, local background issues, non-detection and saturation. Flags are issued for suspect data points. Flux errors are estimated based on the local background noise for all epochs, for all sources. Airmass and differential chromaticity errors are removed by SysREM (Tamuz et al. 2005) in the default pipeline operation; we tested removing explicit correlations with star color and measured airmass, but did not find a significant improvement in photometric precision. These procedures work for the large majority of the data set, but a small fraction ( $<20\%$ ) of the epochs are subject to largely unremovable variability due to thin clouds with spatial scales smaller than a HEALPix pixel. We detect and remove these epochs by searching for periods of higher than average photometric variability among all sources in the healpix, as well as higher than average extinction. We are currently developing methods to instead flag and recover these epochs for usable data.

We have implemented several layers of systematics removal, which can be applied depending on the science goals. All light curves are automatically decorrelated by two iterations of SysREM (Tamuz et al. 2005). Further iterations of SysREM further remove systematic errors, but there is also a risk of removing astrophysical variability. If only short-term variability is to be measured, such as in a transit or eclipse search, we add decorrelations of photometric variability with CCD chip position and airmass. We found that some long-term variables such as low-amplitude long-period rotation curves

correlate with those telescope variables, and so we offer users the option of using uncleaned light curves.

Processed light data is inserted to a PostgreSQL database, also partitioned into HEALPix pixels to increase performance. This database does not include much of the per-epoch metadata, and only contains results from the optimal photometric aperture. Each of the 6000 populated HEALPix pixels contains 0.2–2 GB of light-curve data, for a total light-curve database size of  $\sim 10$  TB. We query the database for target groups, and download the results to Chapel Hill for astrophysical analysis.

### 3. Performance

#### 3.1. Operations Statistics

The Evryscope saw first light on 2015 May 20 and has been operating continually since then with only brief maintenance shutdowns. From first light to 2018 August 1, 15.9% of the nights were missed due to weather and equipment issues, and 2.3% of the nights were skipped due to planned maintenance. The maintenance trips occurred during 2015 November 11–20 (Robotilter installation and camera alignment); 2017 January 4–15 (lens cleaning, data storage increase, second analysis server installation, and general maintenance); and 2018 July 18–25 (lens cleaning and general maintenance). The fail-safe shutdowns occurred for the following reasons: excessive heat warning (20%), dome-control warnings (33%), and smoke/dust/other warning (47%). Almost all of the fail-safe shutdowns were false alarms, but we designed the system to be conservative with the goal of detecting real danger situations at the expense of some false positives.

#### 3.2. Hardware Reliability

The Evryscope has operated reliably for over three years, with only minor hardware issues. The mount has tracked over 5700 2-hour ratchet cycles with no major problems; during the 2017 maintenance trip we greased and tightened the worm gear adjustment which helped smooth the mount operation at peak stress positions. The support structures, including the fiberglass mushroom, have been durable and shown no signs of excessive wear or stress. The power supply units (cameras, filter wheels, servos, USB hubs and accessories) have all performed without issue. The cameras have also run reliably and without failure. Three filter wheels have failed over the course of three years. One broke a drive chain, while the other two stuck during routine cycling. One was stuck in the Sloan-g position so it did not affect imaging, the others were stuck closed so we lost the ability to image with two cameras until the next maintenance trip. One power cable to a camera USB hub failed in mid 2018 which disrupted operation of four cameras and filter wheels; it was easily replaced during the 2018 June maintenance trip. The system is well sealed, and minimal dirt and dust accumulates

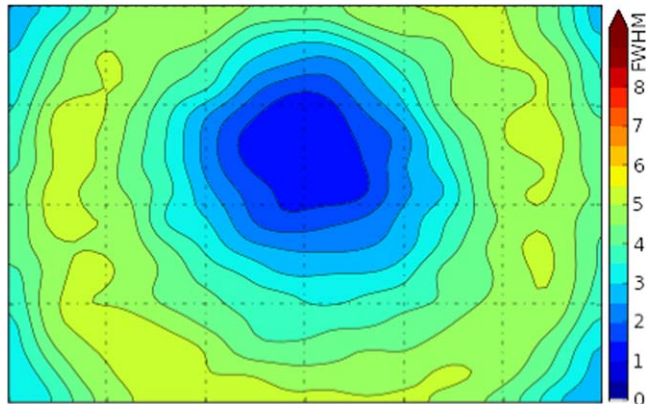


**Figure 12.** FWHM map of the camera pointing toward the South Celestial Pole. The image quality shows little tilt and a symmetric pattern. (A color version of this figure is available in the online journal.)

inside the mushroom. The optical windows need to be manually cleaned each trip, but the lenses can be cleaned simply with compressed air and/or off-the-shelf DSLR camera lens-cleaning pens.

#### 3.3. Imaging Performance

The Evryscope imaging performance sets the limiting magnitude, photometric performance, and ease of source separation and image subtraction. In this subsection we explore the system’s performance over the first three years of operation.

##### 3.3.1. Point Spread Functions

The Robotilter camera/CCD automated alignment system is designed to remove tilt, minimize PSF distortions, optimize the focal plane, and defocus the image center. The PSF FWHM map of a well aligned, representative camera is shown Figure 12). Very little tilt across the image is evident, and PSF widening toward the corners due to lens coma, focus, and vignetting is within the expected range for our lenses. The PSFs range from 1–5 pixel FWHM across much of the image: 60% are less than 4 pixels, and 90% are less than 6 pixels. Figure 13 shows point-spread functions for the central region and edges of a representative camera.

##### 3.3.2. Limiting Magnitudes and Coaddition

We calculate the limiting magnitude achieved by the system in each epoch by taking the faintest stars in each healpix and fitting the S/N decrease as a function of the g-band magnitude as measured by APASS. The dark-sky limiting magnitude (Figure 14) reaches our expectation of  $m_g \approx 16$ , with crowding from the galaxy reducing the limiting magnitude by approximately a magnitude in low-galactic-latitude areas. A horizontal stripe pattern is visible in the limiting-magnitude

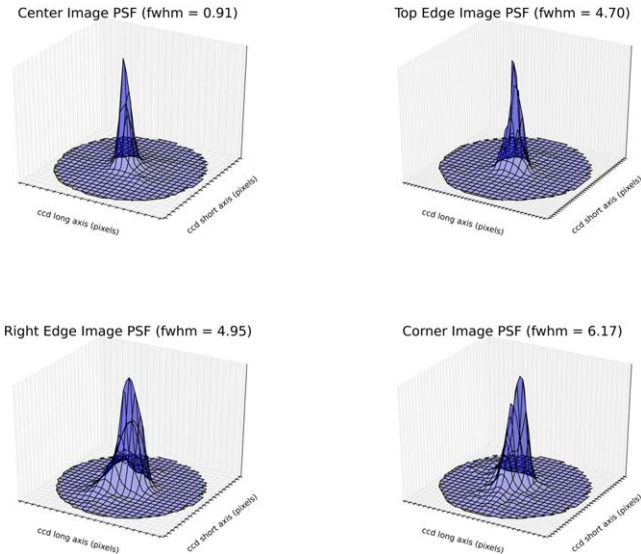


**Figure 13.** Example medium brightness stars' PSFs from the center, edges, and corner of a representative camera.

(A color version of this figure is available in the online journal.)

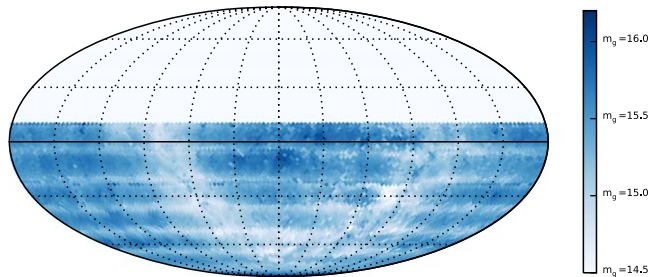


**Figure 14.** Median dark-sky limiting magnitude for Evryscope data, measured in  $\approx 32,000$  epochs over three years of operations. The crowding effects of the galactic plane are visible, along with the striping from falloff in PSF quality toward the edges of the cameras' fields.

(A color version of this figure is available in the online journal.)

map; this is caused by the falloff in PSF quality toward the edge of camera fields of view.

The camera gains, data compression and calibration fidelities are selected so that coadding the data achieves greatly improved S/N, with depth increasing with approximately the square root of the number of exposures (Figure 15). In uncrowded regions of the sky during dark nights, the system typically achieves  $m_{g'} = 17$  in 8 minutes coadding (four exposures),  $m_{g'} = 17.5$  in 32 minutes,  $m_{g'} = 17.8$  in 64 minutes, and  $m_{g'} = 18.5$  in 360 minutes (the latter crowding-limited over much of the sky; see Figure 16).

### 3.3.3. Photometric Precision

Light-curve performance reaches our expected performance levels of near 1% rms on bright stars and  $\sim 10\%$  on dim stars,

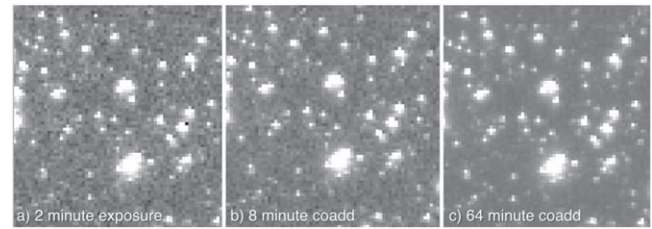


**Figure 15.** Progressive coaddition of a selected sky region, with image scaling applied to show the noise structure in the images. As well as increasing depth, coaddition with the slow star position changes over a ratchet allows the removal of bad and hot pixels.

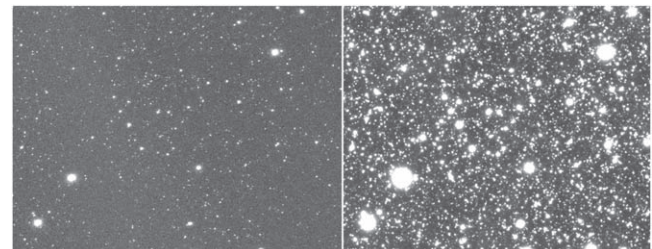


**Figure 16.** Left: a selected region of a single 2-minute Evryscope exposure. Right: coaddition of a full night of data from the same region, with scaling to show the increased number of stars and the bright-star PSFs.

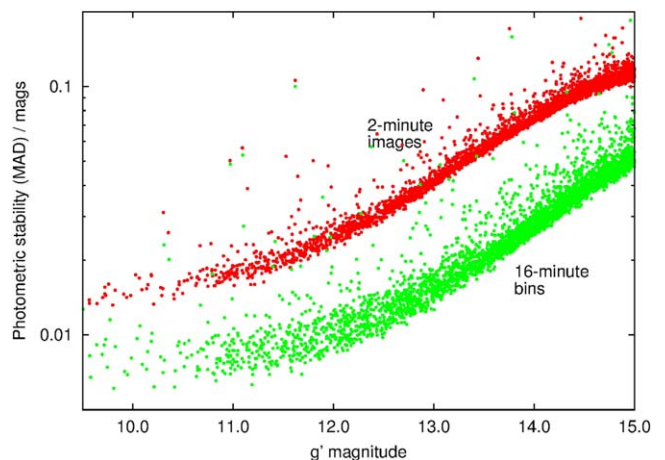


**Figure 17.** Evryscope light-curve photometric performance per magnitude for three years of data under all moon and cloud conditions. Stars in a representative HEALPix pixel of the Evryscope database targets is shown for visual clarity. The high rms outlier points are astrophysical variable stars. (A color version of this figure is available in the online journal.)

over three years of data under all moon and cloud conditions (Figure 17). With binning and/or aggressive removal of poor conditions data and systematics, the performance is improved to the 6-millimag level. These levels are greatly improved when coadding epochs for the detection of periodic objects, where we

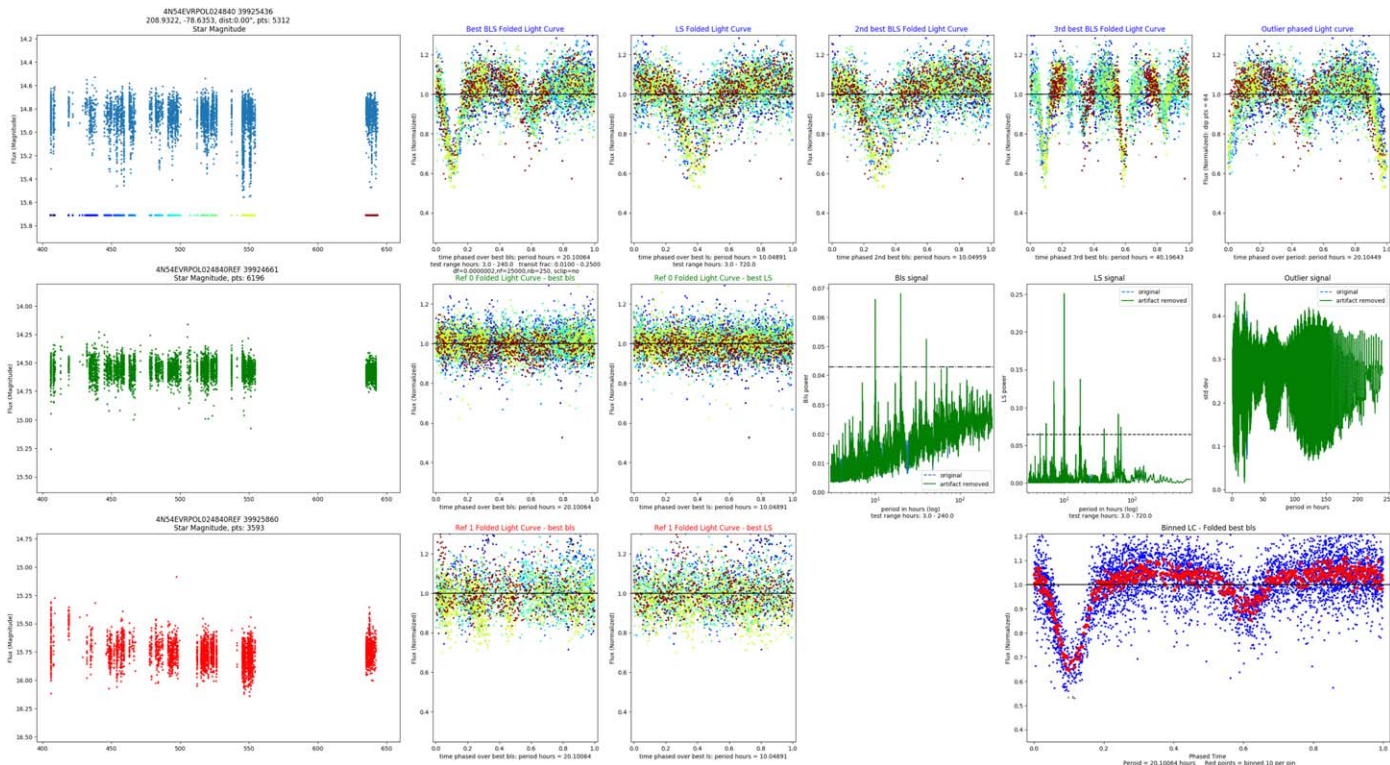


**Figure 18.** Evryscope transit detection display panel, with a newly discovered eclipsing binary. The left panels show the target and two reference star light curves, as well as the BLS and LS phase folded on the best period. The coloring of points shows the mixing of the best period find and comparison to nearby references for identification of systematics. The right panels show the outlier results and the binned light curve folded on the best period. (A color version of this figure is available in the online journal.)

have published clear signals at the few-millimag level (Tokovinin et al. 2018).

#### 4. Example Light Curves, Discoveries, and Ongoing Surveys

The Evryscope has a wide variety of ongoing surveys (Section 2.1). In this section we detail results from some of the current surveys, provide example Evryscope light curves and discoveries from a selected region of the sky; many more comprehensive surveys are currently ongoing.

##### 4.1. Candidate Detection

The Evryscope team uses a wide range of detection tools, given the variety in the science survey goals (see Section 2.1). Box Least Squares (BLS) (Kovacs et al. 2002; Ofir 2014) is the primary search tool used for conventional (wide, shallow, many points) transit like detections. The box size, sampling, and period range are selected depending on the host star and expected companion type. To find potential transiting planets with compact host stars such as white dwarfs or hot subdwarfs, where the transit times are orders of magnitude shorter, we developed a custom code written in Python which we call the

outlier detector. It excels in finding very short time (on the order of a few minutes to tens of minutes) transits with deep (10% or more) depths, even for faint objects. We use several iterative processes to select low outlying points and find the period with lowest in phase deviation. Flares are discovered and characterized with an automated flare-analysis pipeline which uses a custom flare-search algorithm, including injection tests to measure the flare recovery rate. The algorithm searches for flares by first dividing each light curve into segments of continuous observations and subsequently fitting an exponential-decay matched-filter to each contiguous segment of the light curve. Matches with a significance greater than  $4.5\sigma$  are verified by eye. Microlensing events are detected with a differential image/matched-filter Python code that triggers an alert if required parameters are met. Lomb-Scargle (LS) (Lomb 1975; Scargle 1982) is the primary algorithm used to find stellar variability and binaries.

Visual inspection and systematic assessment is a key to detection and false-positive elimination. We have developed several visual tools including the display panel plot (Figure 18) that allows for simple and effective visual confirmation of candidates. In the same panel plot, we test the candidates for signs of systematics by comparisons to nearby reference stars,

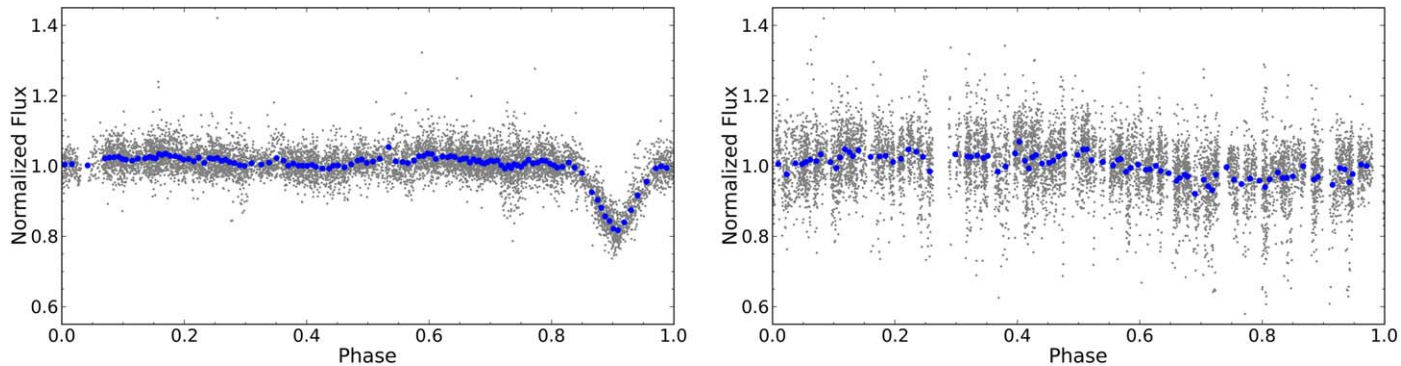


**Figure 19.** Left: an eclipsing binary discovery folded on its 61.4905 hour period representative of 100's of Evryscope variable discoveries. Right: a variable star discovery folded on its 219.8386 hour period representative of 100's of Evryscope variable discoveries.

(A color version of this figure is available in the online journal.)

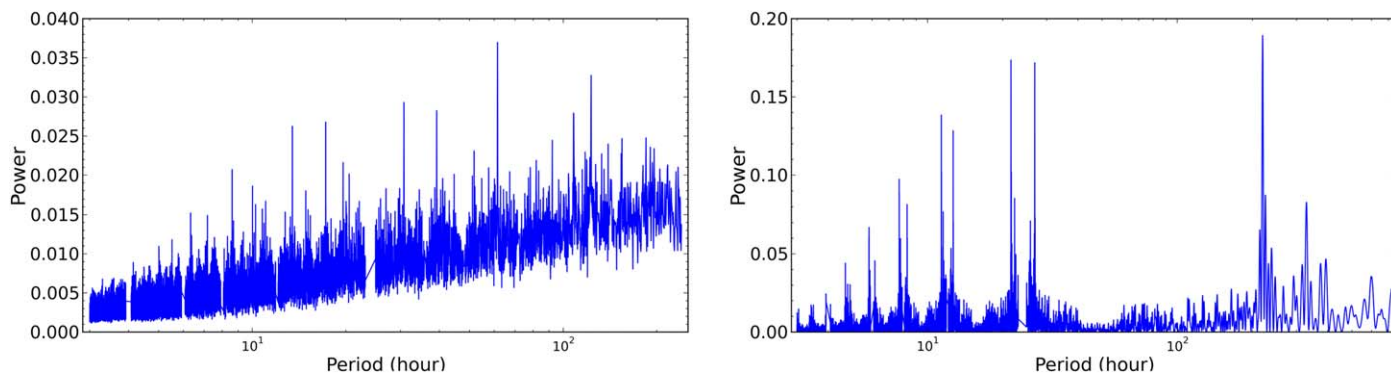


**Figure 20.** Left: the BLS power spectrum (to the 61.4905 hour eclipse in Figure 19) with the highest peak at the 61.4905 hour detection. Right: the LS power spectrum (to the 219.8386 hour variable star in Figure 19) with the highest peak at the 219.5521 hour detection.

(A color version of this figure is available in the online journal.)

examining binned data, and checking for alias and data gaps. Fit power, ordering, and selection of top targets is available to narrow the candidates depending on the search and number of targets. This display is available for all Evryscope light curves on request.

#### 4.2. First Discoveries

The Evryscope team (and collaborators from 17 institutions) are engaged in a wide variety of astrophysical projects with the light-curve data set. The first major Evryscope result, the first detection of a superflare from Proxima Centauri, was recently published in *ApJL* (Howard et al. 2018). Several other papers are currently under review, and many more results in preparation. Here, we show some examples of variability discoveries from the Evryscope database, and results from a test search in a selected region of the sky. We follow with updates on the various surveys that are underway.

##### 4.2.1. New Eclipsing Binary/Variable Star Discoveries

A test search limited to the northern region (declinations from +5 to +10), filtering the targets by magnitude (bright stars) and color (likely K-dwarfs or M-dwarfs) yielded 59 new eclipsing binaries and variables. Representative examples of an eclipsing binary and a low-amplitude variable are shown in Figure 19. The search was run by selecting all of the sources in the Evryscope database with light curves with greater than 5000 epochs, with magnitudes brighter than 14.5, and with sources that matched to PPMXL (Roeser et al. 2010) and APASS-DR9 (Henden et al. 2015) catalogs which could be classified as potential K-dwarf or M-dwarfs based on reduced proper motion (RPM) and B-V colors. After removing known variables, BLS and LS were run on the filtered list; the example eclipsing binary and low-amplitude variable BLS and LS detections are shown in Figure 20. The BLS and LS results were ordered by significance and the top 10% were inspected using the detection panel plots. Those passing the visual



**Table 4**  
Variable Star Discoveries

ESID	APASS ID	R.A.	Decl.	$M_v$	RPM	B-V	Size	Spec	Period (hours)	Amplitude (delta mag)
EVRJ013131.44+061855.1	16891108	22.8810	6.3153	12.99	11.22	0.97	ms	K3V	56.0725	0.047
EVRJ024227.96+062556.3	53362	40.6165	6.4323	13.01	10.56	1.09	ms	K7V	3.3478	0.047
EVRJ031204.99+073711.3	41698	48.0208	7.6198	13.40	10.22	1.13	ms	K7V	34.9678	0.076
EVRJ031736.19+080644.3	34215	49.4008	8.1123	12.65	10.37	1.05	ms	K5V	10.5253	0.048
EVRJ033741.28+064752.1	23523707	54.4220	6.7978	11.28	11.24	0.88	ms	G9V	4.5936	0.018
EVRJ040342.82+051630.0	23508836	60.9284	5.2750	12.50	9.36	1.06	ms	K4V	30.5414	0.028
EVRJ055815.07+082912.5	23801506	89.5628	8.4868	13.65	9.03	1.14	giant	K5	22.9847	0.047
EVRJ062900.94+075330.8	23826908	97.2539	7.8919	11.86	9.20	0.85	ms	K2V	136.1824	0.053
EVRJ063213.30+063835.2	22292962	98.0554	6.6431	14.31	9.77	0.86	ms	G	161.5992	0.165
EVRJ064304.61+080711.6	22342837	100.7692	8.1199	11.90	6.36	1.29	giant	K	3.2894	0.050
EVRJ074608.52+064450.3	22513221	116.5355	6.7473	13.81	9.04	0.96	ms	K3V	4.1063	0.068
EVRJ090345.07+063356.5	5090425	135.9378	6.5657	13.27	10.18	0.85	ms	K2V	1001.4160	0.041
EVRJ133939.43+080936.4	26935380	204.9143	8.1601	13.00	10.44	0.87	ms	K2V	3.5490	0.050
EVRJ135123.76+074111.4	26926300	207.8490	7.6865	12.47	11.84	0.93	ms	K3V	103.5052	0.048
EVRJ150518.17+062323.6	7678546	226.3257	6.3899	13.36	9.98	0.96	ms	K3V	4.0030	0.053
EVRJ153240.92+054336.1	34080751	233.1705	5.7267	11.60	11.04	0.92	ms	K4V	29.5485	0.021
EVRJ153936.96+061720.8	34088653	234.9040	6.2891	12.61	9.49	1.00	ms	K3V	1408.9650	0.057
EVRJ155120.62+061448.8	34085878	237.8359	6.2469	13.56	9.81	1.22	ms	K6V	106.1767	0.047
EVRJ155543.75+062518.8	34071112	238.9323	6.4219	11.24	12.09	1.04	ms	K4V	29.7894	0.031
EVRJ164449.03+082109.7	34208168	251.2043	8.3527	13.36	11.12	0.98	ms	K5V	33.4419	0.052
EVRJ173918.65+081931.4	34776606	264.8277	8.3254	13.32	6.90	0.95	giant	K	6.0188	0.013
EVRJ175437.66+061028.2	34517257	268.6569	6.1745	14.08	11.47	0.88	ms	G	13.2881	0.079
EVRJ180850.26+073350.4	34512011	272.2094	7.5640	13.48	15.00	1.09	ms	K2V	3.8693	0.069
EVRJ182013.44+083523.6	34587201	275.0560	8.5899	12.23	7.27	1.28	giant	K	197.7393	0.040
EVRJ182020.76+065445.0	34568159	275.0865	6.9125	13.25	9.71	1.10	ms	K5V	183.1411	0.063
EVRJ183036.48+073707.7	34556082	277.6520	7.6188	13.19	10.64	0.86	ms	K1V	3.8968	0.077
EVRJ184426.98+073442.2	32193828	281.1124	7.5784	13.44	10.15	0.87	ms	G0V	4.9937	0.133
EVRJ190325.54+071516.9	32730341	285.8564	7.2547	11.47	9.05	0.98	ms	K3V	243.1183	0.017
EVRJ190353.14+051812.6	32116381	285.9714	5.3035	13.33	9.38	1.04	ms	K3V	4.0273	0.052
EVRJ190517.30+073520.0	32730666	286.3221	7.5889	13.62	12.11	1.30	ms	K7V	15.7103	0.041
EVRJ190632.06+051345.5	32715501	286.6336	5.2293	12.64	9.27	1.19	giant	K7	13.0606	0.080
EVRJ191341.81+070205.6	32721487	288.4242	7.0349	13.32	11.73	1.09	ms	K3V	12.3459	0.014
EVRJ191731.06+070124.6	32722226	289.3794	7.0235	12.46	11.20	1.03	ms	K4V	219.8386	0.037
EVRJ191757.24+090428.2	32747699	289.4885	9.0745	14.30	11.60	0.87	ms	G	22.4846	0.070
EVRJ191908.38+083523.6	32746157	289.7849	8.5899	14.37	11.70	0.95	ms	K	136.0364	0.059
EVRJ193728.03+054802.2	32326983	294.3668	5.8006	13.09	9.30	0.86	ms	G9V	16.6612	0.034
EVRJ194947.38+060847.8	32478891	297.4474	6.1466	12.92	11.65	0.88	ms	K2V	5.8423	0.123
EVRJ195419.58+084303.0	32521135	298.5816	8.7175	13.75	7.11	1.14	giant	K	236.7087	0.022
EVRJ195728.85+074311.6	32498119	299.3702	7.7199	14.01	10.39	1.27	ms	K6V	4.5788	0.033
EVRJ201533.41+082530.4	31613658	303.8892	8.4251	12.64	13.07	0.94	ms	K4V	28.9305	0.052
EVRJ203320.59+090539.8	9498741	308.3358	9.0944	14.00	10.32	0.91	ms	K2V	3.1976	0.105
EVRJ204952.97+054416.1	9315264	312.4707	5.7378	12.97	9.25	0.91	ms	K3V	161.5235	0.088
EVRJ210125.78+082428.8	9339138	315.3574	8.4080	...	...	...	none	none	20.9755	0.018
EVRJ211939.26+065648.5	9353342	319.9136	6.9468	12.90	9.18	1.09	ms	K3V	28.1581	0.038
EVRJ230853.71+071107.1	17248213	347.2238	7.1853	13.14	11.38	1.09	ms	K6V	12.5262	0.139

**Note.** Columns 1–5 are identification numbers, right ascension and declination, and magnitude. Columns 6–9 are the reduced proper motion (RPM) and color difference (B-V) which we use to estimate the star size and spectral type (see Section 4.2.1). Columns 10 and 11 are the period found in hours, and the amplitude of the variability in magnitudes.

inspection and systematics test were sent to the next stage. Eclipsing Binaries were fit with a Gaussian to measure the eclipse depth using the detected period and phase as the prior. Variables were fit using Lomb-Scargle to determine the

amplitude. Example eclipsing binary and low-amplitude variable fits are shown in Figure 21. Tables 4–6 in the Appendix contain the full discovery list; Figures 22 and 23 display the light curves.

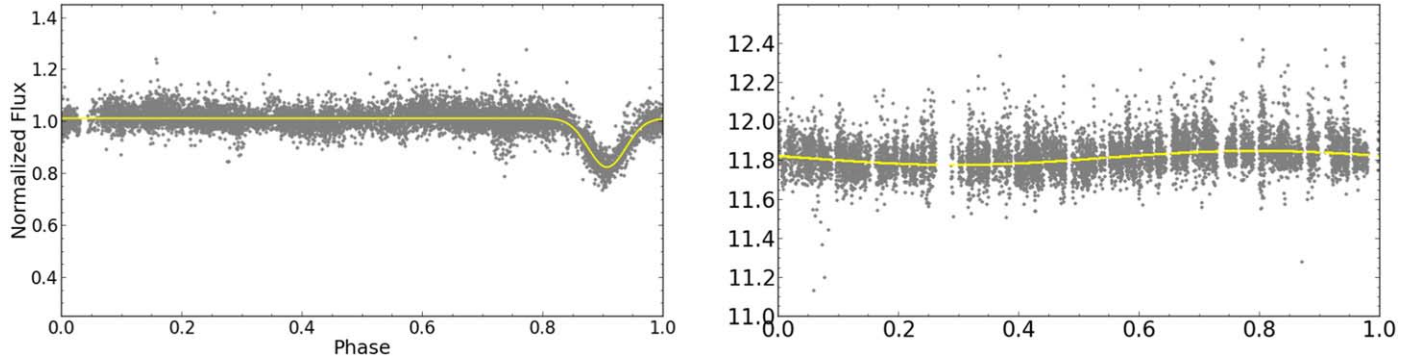


**Figure 21.** Left: the best fit (to the 61.4905 hour eclipse in Figure 19) to measure the depth. Gray points are 2-minute cadence, red points are binned in phase, yellow is the best Gaussian fit. Right: the best fit (to the 219.8386 hour variable star in Figure 19) to measure the amplitude. Gray points are 2-minute cadence, red points are binned in phase, yellow is the best LS fit.

(A color version of this figure is available in the online journal.)

**Table 5**  
Transient Discovery

ESID	APASS ID	R.A.	Decl.	$M_v$	RPM	B-V	Size	Spec	Duration (days)	Amplitude (delta mag)
EVRJ194754.19+073408.0	32510284	296.9758	7.5689	14.040	10.895	1.450	ms	M1V	100	1.5

**Table 6**  
Eclipsing Binary Discoveries

ESID	APASS ID	R.A.	Decl.	$M_v$	RPM	B-V	Size	Spec	Period (hours)	Depth (fractional)
EVRJ054324.82+070043.6	24006556	85.8534	7.0121	14.42	8.78	1.07	ms	K	12.3630	0.415
EVRJ062259.52+050915.8	23805977	95.7480	5.1544	14.14	9.80	1.28	ms	M0.5V	159.7402	0.286
EVRJ111947.62+085811.6	27552269	169.9484	8.9699	14.02	10.41	0.97	ms	K3V	56.7865	0.385
EVRJ171609.43+070050.0	33836552	259.0393	7.0139	12.75	10.00	0.93	ms	K3V	16.0351	0.236
EVRJ180755.37+063452.0	34507331	271.9807	6.5811	14.12	7.27	1.20	giant	K	51.7911	0.111
EVRJ181019.32+083846.3	34654251	272.5805	8.6462	14.23	7.54	1.14	giant	A1	32.6179	0.166
EVRJ181348.53+071553.6	34574081	273.4522	7.2649	13.87	11.70	0.89	ms	G	16.4074	0.145
EVRJ182614.59+053454.1	34537571	276.5608	5.5817	13.21	10.93	1.15	ms	K	19.6076	0.160
EVRJ191419.87+083226.5	32745386	288.5828	8.5407	14.23	9.78	0.95	ms	K	61.4905	0.189
EVRJ192207.27+084849.7	32743749	290.5303	8.8138	14.15	9.82	0.98	ms	K4V	25.9350	0.196
EVRJ194419.61+072333.4	32508956	296.0817	7.3926	...	...	...	...	...	18.5312	0.279
EVRJ201131.20+061020.6	31583110	302.8800	6.1724	14.01	9.45	1.07	ms	K4V	15.1673	0.224
EVRJ201329.93+050717.0	31577212	303.3747	5.1214	11.81	9.97	0.88	ms	G7V	213.0682	0.093
EVRJ202807.01+053621.2	31532342	307.0292	5.6059	14.29	11.00	1.12	ms	K5V	28.2712	0.094

**Note.** Columns 1–5 are identification numbers, right ascension and declination, and magnitude. Columns 6–9 are the reduced proper motion (RPM) and color difference (B-V) which we use to estimate the star size and spectral type (see Section 4.2.1). Columns 10 and 11 are the period found in hours, and the fractional eclipse depth from normalized flux.

#### 4.2.2. Transit Surveys

One major Evryscope transit survey has been completed and two are underway, with several others in the planning stages. A transit search for variable stars in the southern polar region led to 300 variable and eclipsing binary discoveries, with six of the eclipsing binaries having low-mass secondaries (Ratzloff et al. 2019). An exoplanet survey of  $\approx 2500$  southern sky white

dwarf (WD) targets  $m_v < 15.0$  is underway. A transit survey of  $\approx 3500$  hot subdwarf (HSD) targets is in progress and has already discovered several rare systems: 2 HSD/low-mass-secondary eclipsing binaries (HW Vir systems), 4 HSD reflection binaries, and 2 HSD/WD short-period binaries (J. K. Ratzloff et al. 2019, in preparation). From these surveys, there have been five planet candidate detections; subsequent

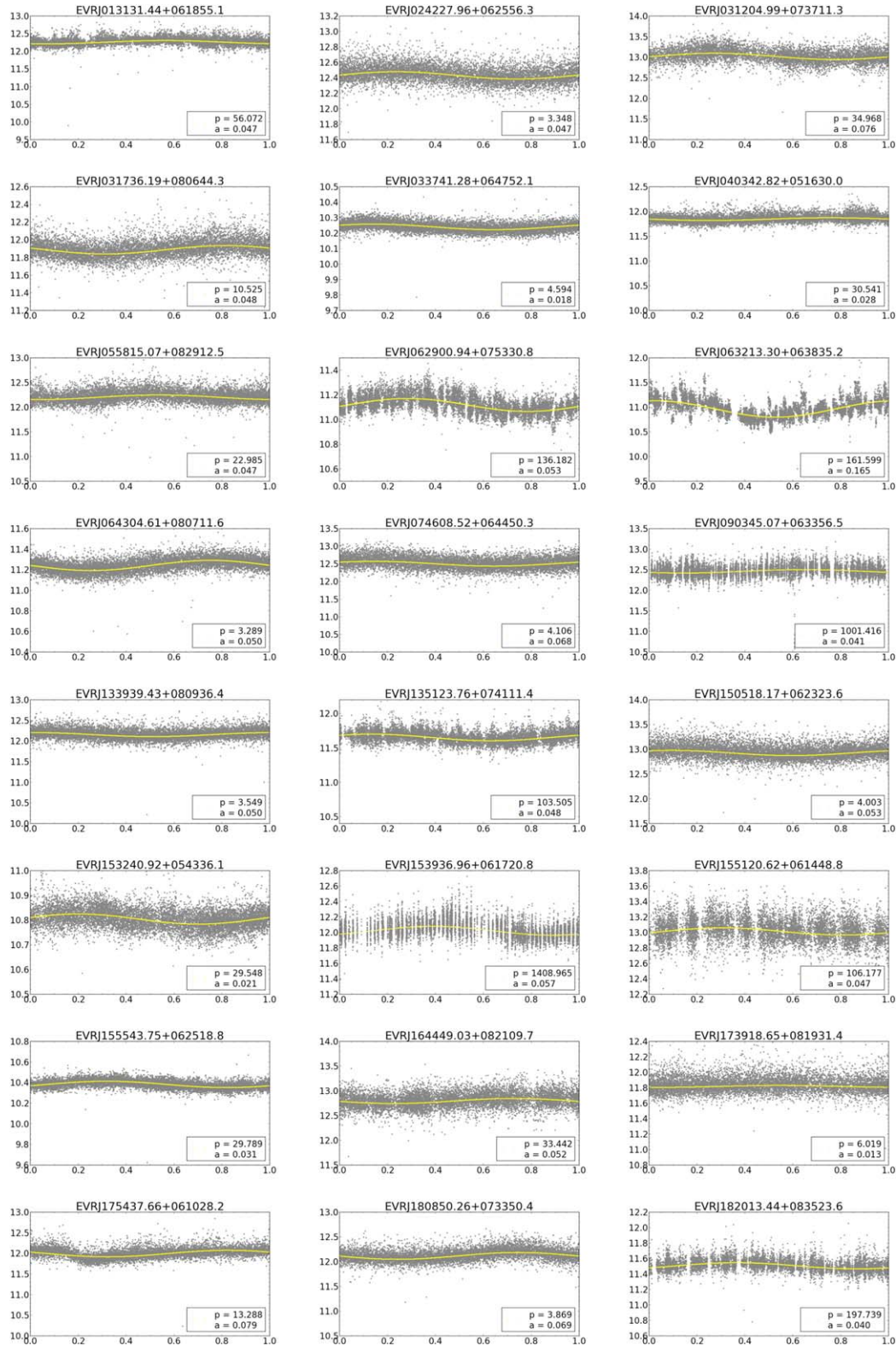


**Figure 22.** (a) Variable star discoveries. Y-axis is instrument magnitude, x-axis is the phase,  $p$  = period found in hours,  $a$  = amplitude change in magnitude. Gray points are 2-minute cadence, yellow is the best LS fit. (b) Variable star discoveries (continued). Y-axis is instrument magnitude, x-axis is the phase,  $p$  = period found in hours,  $a$  = amplitude change in magnitude. Gray points are 2-minute cadence, yellow is the best LS fit. (A color version of this figure is available in the online journal.)

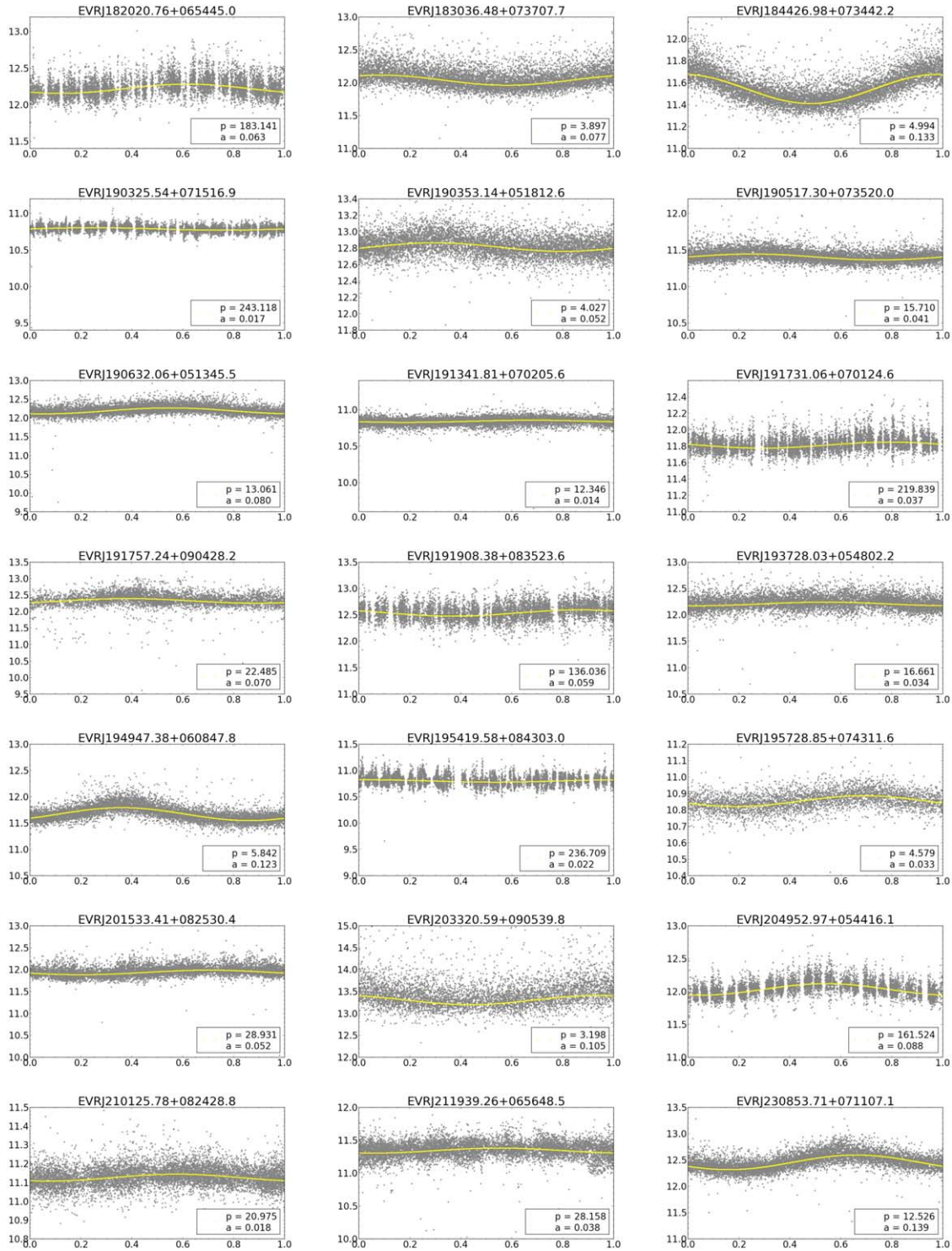
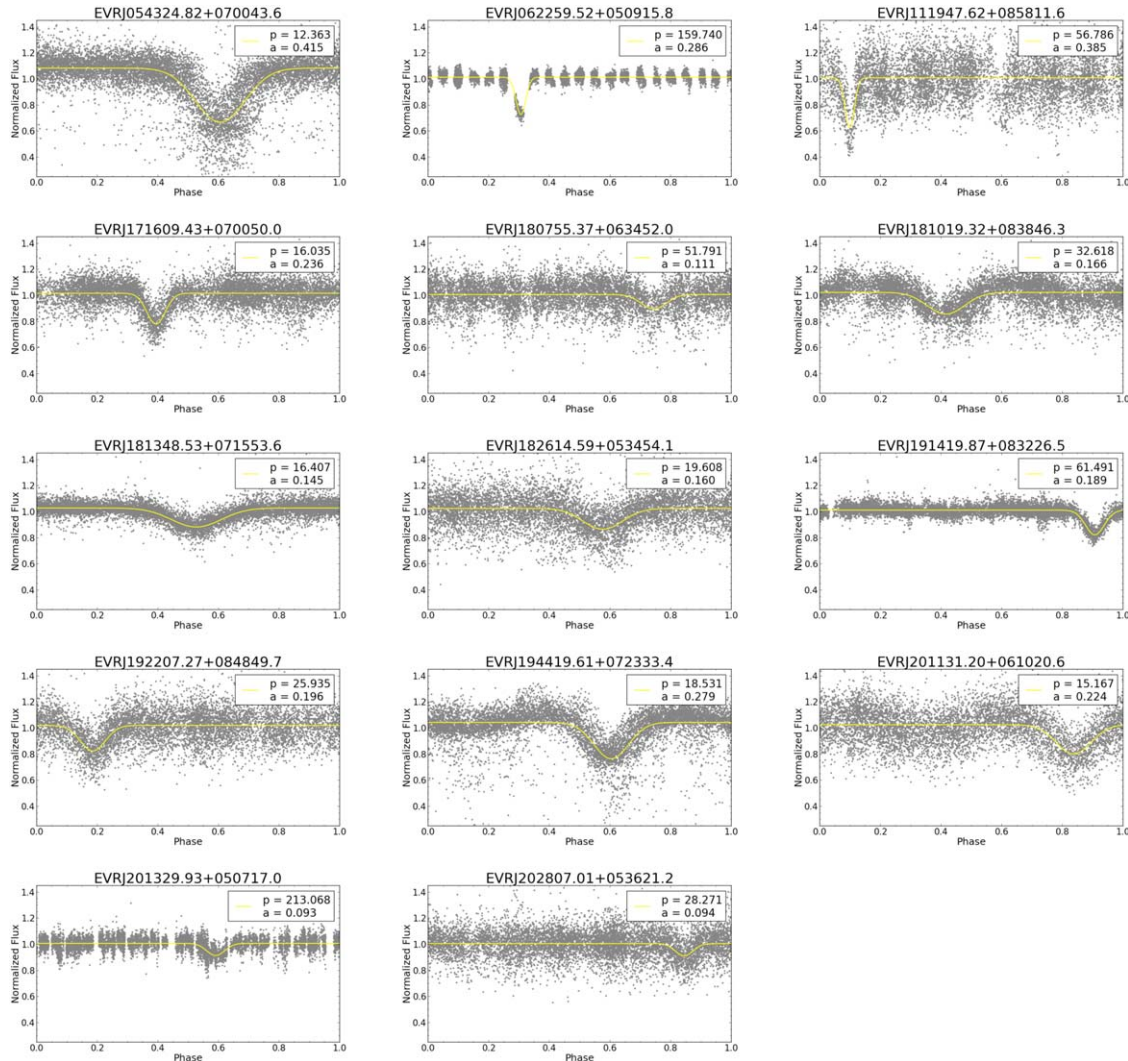


Figure 22. (Continued.)



**Figure 23.** Eclipsing Binary discoveries. Y-axis is normalized flux, x-axis is the phase,  $p$  = period found in hours,  $a$  = eclipse depth. Gray points are 2-minute cadence, yellow is the best fit.

(A color version of this figure is available in the online journal.)

follow-up showed these candidates to be grazing eclipsing binaries with almost identical stars or low-mass stellar companions. These detections demonstrate the Evryscope is capable of detecting planets orbiting post main-sequence stars as well as M and K-dwarfs with our current light curves and search algorithms. We have used the initial results of these first surveys to refine our transit searches; we briefly describe the status of the key Evryscope transit surveys below.

*White dwarfs (WD).* Recent discoveries of WD debris disks and disintegrating planetesimals have fueled the speculation that planets could be present in WD systems (Loeb & Maoz 2013; Veras et al. 2018). WD exoplanets would have very short (few minutes to tens of minutes) transit duration and very deep ( $\sim 100\%$  for Earth-size planets) transit depths. WDs are extremely numerous in the sky as  $>90\%$  of main-sequence

stars will eventually become WDs, however the low luminosity and small size make these stars observationally challenging. We leverage the Evryscope fast cadence and all-sky coverage to search for WD planets. Our first results from  $\approx 2500$  southern sky WD targets  $m_v < 15.0$  did not return any candidates. We have improved our systematics removal, increased our coverage to 3.5 years, and added targets down to  $m_v < 16.0$  and will search again once the database processing is complete (J. K. Ratzloff et al. 2019, in preparation). In the event of a null detection, we can provide upper limit constraints on WD planetary populations.

*Hot subdwarfs (HSD).* HSD planet or low-mass-secondary transit durations are on the order of tens of minutes, and reasonably deep transit depths ( $\sim 10\%$  for Neptune size planets). A transit survey of HSD planets and other variability

from a target list (Geier et al. 2017) of  $\approx 3500$  known HSD is in progress (J. K. Ratzloff et al. 2019, in preparation). Although the survey is currently underway, several candidates, including the 8 mentioned above, have been identified and are pending further follow-up.

*M- and K-dwarfs.* The Evryscope is capable of detecting  $\sim 2$  Earth radii M-dwarf planets and gas giant K-dwarf planets. A transit search for variable stars in the southern polar region detected a  $1.7 R_J$  planet candidate with a late K-dwarf primary. This system was later shown to be a grazing eclipsing binary, but demonstrated the Evryscope detection capability. An exoplanet survey of M and K-dwarf stars based on identifying candidates in our fields from spectral classification is planned for the entire sky when the HSD and WD surveys are completed.

### 4.3. Other Variability Searches

#### 4.3.1. Solar Flares and CME

Flares and coronal mass ejections (CMEs) are capable of severely affecting the survivability of potentially habitable worlds. A comprehensive flare survey of M-dwarf stars (including known exoplanet hosts) of the southern sky is underway (W. Howard et al. 2019, in preparation). These results, when combined with CME observations will be used to estimate the effects on long-term habitability of rocky planets orbiting M-dwarf stars.

#### 4.3.2. Transient Detection

We have developed tools for rapidly generating small cutouts from full-frame Evryscope images and performing high-precision photometry on uncataloged sources not included in our primary forced-photometry reduction, including difference image analysis for objects in crowded regions of the sky. This tool chain is designed to provide early prediscovery photometry to help constrain the evolution of novae and supernovae.

An example of Evryscope transient capability is a recent classical nova (Nova Carinae 2018) with prediscovery Evryscope coverage (Corbett et al. 2018), which is currently under analysis and a detailed light curve will be presented in an upcoming paper (H. Corbett, et al. 2019, in preparation). The Evryscope data complements the later discovery by the All Sky Automated Survey for SuperNovae (ASASSN; Stanek et al. 2018) and the serendipitous space-based photometry of the Bright Target Explorer (BRITE Kuschnig et al. 2018). High-cadence and high-coverage observations of classical novae can provide insight into the shock physics that drive light-curve evolution (Li et al. 2017). Also shown in Figure 24 is transient discovery from the variable star test search (Section 4.2.1).

## 5. Summary

The Evryscope was deployed to CTIO in 2015 May and has recently been joined by a northern-hemisphere telescope at MLO. The Evryscope is designed to detect short-timescale events across

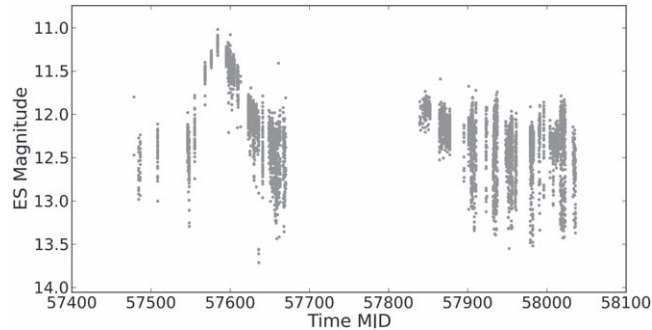


**Figure 24.** Transient discovery with  $\sim 100$  day duration and 1.5 magnitude increase. Other long-period variables and transients including supernovae, novae, and microlensing events are detectable with the Evryscope.

extremely large sky areas simultaneously. The 780 MPix 22-camera array has an 8150 sq. deg. FoV, 2-minute cadence, and the ability to detect objects down to  $m_{g'} \simeq 16$  in each dark-sky exposure. We have collected over 250 TB of images and produced 25 TB of light curves. In this paper, we described the Evryscope hardware and explained why we designed the telescope as we did. The time from conceptual design to deployment was one year and the total hardware cost was  $\approx \$300k$ , meeting our time and budgetary goals. We demonstrated the on-sky performance met our goals for telescope operation and reliability, sky tracking, threat mitigation, and reliability. Image quality reached our predictions for signal, noise, background, and PSF quality. The photometric pipeline produces light curves with the precision necessary to support the planned Evryscope science. We demonstrated the photometric performance by presenting select variable star discoveries and discussing rare hot subdwarf and white dwarf eclipsing binary discoveries. Updates on the status of our transit surveys, M-dwarf flare survey, and transient detection were also given.

This research was supported by the NSF CAREER grant AST-1555175, NSF/ATI grant AST-1407589, and the Research Corporation Scialog grants 23782 and 23822. H.C. is supported by the NSF GRF grant DGE-1144081. O.F. and D.d.S. acknowledge support by the Spanish Ministerio de Economía y Competitividad (MINECO/FEDER, UE) under grants AYA2013-47447-C3-1-P, AYA2016-76012-C3-1-P, MDM-2014-0369 of ICCUB (Unidad de Excelencia ‘María de Maeztu’).

## Appendix

### Polar Alignment Procedure for an Extremely Wide-field Telescope

The Evryscope’s extremely wide FoV precludes the use of a pointing/tracking model, because a conventional model optimizes the performance at the sky position at which the telescope is pointing, at the expense of the sky areas away from that direction. The Evryscope effectively points every direction

simultaneously, and so the system's polar alignment accuracy is critical for the tracking performance. Conventional polar alignment strategies are made difficult because of the large pixel scale and lack of ability to point individual cameras in a wide variety of positions.

We instead developed a polar alignment procedure that takes advantage of the Evryscope's extremely wide FoV to produce rapid subarcminute-precision alignment. The procedure uses the polar-facing camera to measure both the axis of rotation of the Earth and the axis of rotation of the telescope mount. Iteratively moving the telescope axis then brings the two into alignment; both axes can be measured to within a few-pixel precision. We perform the alignment as follows:

1. Measure the Earth's axis of rotation on the pole-facing camera by taking a long-exposure image with tracking turned off (10–15 minutes). The Earth's rotation axis position is measured in image coordinates using the center of the star trails. The longer the exposure, the greater the achieved positioning accuracy.
2. Measure the mount's axis of rotation by taking a short-exposure image with the mount moving rapidly ( $\sim$ greater than 20X tracking rate). The motion of the stars is then dominated by the mount rotation, and the center of the star trails is approximately the center of rotation of the mount (with a small offset from the Earth's rotation during the exposure).
3. Iterate on the mount's polar alignment settings to bring the mount rotation axis closer to the Earth's rotation axis. It is sufficient to follow the improvements simply in pixel coordinates on the polar-facing camera. As the axes align, the offset induced by the residual Earth rotation during the mount axis alignment tends to zero, and so the mount's alignment tends to the correct position.

We found that this procedure could be completed in less than two hours with subarcminute-level alignment. This alignment procedure aligns the mount's polar axis but does not precisely locate the celestial pole in the center of the polar camera's FoV; this can be performed later by simply adjusting the mushroom pointing direction.

## References

- Bakos, G., Noyes, R. W., Kovács, G., et al. 2004, *PASP*, **116**, 266
- Bellm, E. C. 2018, arXiv:1802.10218
- Bertin, E., & Arnouts, S. 1996, *A&AS*, **117**, 393
- Corbett, H., Law, N., Goeke, E., et al. 2018, ATel, **11467**, 1
- Corcoran, K. A., Barlow, B., Corbett, H., et al. 2018, AAS Meeting 231, **150.23**
- Csépany, G., Pál, A., Vida, K., et al. 2013, in ASP Conf. Ser. 475, *Astronomical Data Analysis Software and Systems XXII*, ed. D. N. Friedel (San Francisco, CA: ASP), **369**
- Djorgovski, S. G., Drake, A. J., Mahabal, A. A., et al. 2011, arXiv:1102.5004
- Geier, S., Østensen, R. H., Nemeth, P., et al. 2017, *OAsT*, **26**, 164
- Gorski, K. M., Hivon, E., Banday, A. J., et al. 2005, *ApJ*, **622**, 759
- Henden, A. A., Levine, S., Terrell, D., & Welch, D. L. 2015, AAS Meeting 225, **336.16**
- Howard, W. S., Tilley, M. A., Corbett, H., et al. 2018, *ApJL*, **860**, L30
- Kaiser, N., Burgett, W., Chambers, K., Denneau, L., & Heasley, J. 2010, *Proc. SPIE*, **7733**, 77330E
- Keller, S. C., Schmidt, B. P., Bessell, M. S., et al. 2007, *PASA*, **24**, 1
- Kosiarek, M. R., Crossfield, I. J. M., Hardegree-Ullman, K. K., et al. 2019, *AJ*, **157**, 97
- Kovacs, G., Zucker, S., & Mazeh, T. 2002, *A&A*, **391**, 369
- Kuschnig, R., Pigulski, A., Moffat, A. F. J., et al. 2018, ATel, **11508**, 1
- Lang, D., Hogg, D. W., Mierle, K., Blanton, M., & Roweis, S. 2010, *AJ*, **139**, 1782
- Law, N. M., Carlberg, R., Salbi, P., et al. 2013, *AJ*, **145**, 58
- Law, N. M., Fors, O., Ratzloff, J., et al. 2015, *PASP*, **127**, 234
- Law, N. M., Fors, O., Ratzloff, J., et al. 2016, *Proc. SPIE*, **9906**, 99061M
- Law, N. M., Kulkarni, S. R., Dekany, R. G., et al. 2009, *PASP*, **121**, 1395
- Law, N. M., Sivanandam, S., Murowinski, R., et al. 2012, *Proc. SPIE*, **8444**, 84445C
- Lewis, Peter M., & Howard Rogers, R. H. S. 2010, *Proc. SPIE*, **7735**, 77353C
- Li, K.-L., Metzger, B. D., Chomiuk, L., et al. 2017, *NatAs*, **1**, 697
- Loeb, A., & Maoz, D. 2013, *MNRAS*, **432**, L11
- Lomb, N. R. 1975, *Ap&SS*, **39**, 447
- McCullough, P. R., Stys, J. E., Valenti, J. A., et al. 2005, *PASP*, **117**, 783
- Ofir, A. 2014, *A&A*, **561**, A138
- Pai, C., Grossman, S., & Huang, J. 1989, *Adv. Polym. Technol.*, **2**, 157
- Pepper, J., Pogge, R. W., DePoy, D. L., et al. 2007, *PASP*, **119**, 923
- Piotrowski, L. W., Batsch, T., Czyrkowski, H., et al. 2013, *A&A*, **551**, A119
- Pollacco, D. L., Skillen, I., Collier Cameron, A., et al. 2006, *PASP*, **118**, 1407
- Ratzloff, J. K., et al. 2019, *PASP*, submitted
- Reichart, D., Nysewander, M., Moran, J., et al. 2005, *NCimC*, **28**, 767
- Roeser, S., Demleitner, M., & Schilbach, E. 2010, *AJ*, **139**, 2440
- Scargle, J. D. 1982, *ApJ*, **263**, 835
- Shappee, B., Prieto, J., Stanek, K. Z., et al. 2014, AAS Meeting 223, **236.03**
- Stanek, K. Z., Holoiien, T. W.-S., Kochanek, C. S., et al. 2018, ATel, **11454**, 1
- Tamuz, O., Mazeh, T., & Zucker, S. 2005, *MNRAS*, **356**, 1466
- Tokovinin, A., Corbett, H., Fors, O., et al. 2018, *AJ*, **156**, 120
- Tonry, J. L. 2011, *PASP*, **123**, 58
- Tonry, J. L., Stubbs, C. W., Lykke, K. R., et al. 2012, *ApJ*, **750**, 99
- Veras, D., Xu, S., & Rebassa-Mansergas, A. 2018, *MNRAS*, **473**, 2871